Colloquium

Electronic properties and quantum transport in Graphene-based nanostructures

S.M.-M. Dubois, Z. Zanolli, X. Declerck, and J.-C. Charlier[a]

Université catholique de Louvain, Unité de Physico-Chimie et de Physique des Matériaux (PCPM), European Theoretical Spectroscopy Facility (ETSF), Place Croix du Sud 1, 1348 Louvain-la-Neuve, Belgium

Abstract. Carbon nanotubes (CNTs) and graphene nanoribbons (GNRs) represent a novel class of low-dimensional materials. All these graphene-based nanostructures are expected to display the extraordinary electronic, thermal and mechanical properties of graphene and are thus promising candidates for a wide range of nanoscience and nanotechnology applications. In this paper, the electronic and quantum transport properties of these carbon nanomaterials are reviewed. Although these systems share the similar graphene electronic structure, confinement effects are playing a crucial role. Indeed, the lateral confinement of charge carriers could create an energy gap near the charge neutrality point, depending on the width of the ribbon, the nanotube diameter, the stacking of the carbon layers regarding the different crystallographic orientations involved. After reviewing the transport properties of defect-free systems, doping and topological defects (including edge disorder) are also proposed as tools to taylor the quantum conductance in these materials. Their unusual electronic and transport properties promote these carbon nanomaterials as promising candidates for new building blocks in a future carbon-based nanoelectronics, thus opening alternatives to present silicon-based electronics devices.

PACS. 61.46.-w Structure of nanoscale materials – 73.63.-b Electronic transport in nanoscale materials and structures

1 Introduction

Carbon nanomaterials reveal a rich polymorphism of various allotropes exhibiting each possible dimensionality: fullerene molecule (0D), nanotubes and graphene ribbons (1D), graphite platelets (2D), and nano-diamond (3D) are selected examples. Because of this extraordinary versatility of nanomaterials exhibiting different physical and chemical properties, carbon nanostructures are playing an important role in nanoscience and nanotechnology.

The fundamental building block in these carbon nanostructures (except for sp^3 diamond) relies on the theoretical concept of the graphene sheet. Indeed, graphene is the name given to a perfect infinite single layer of sp^2-bonded carbon atoms densely packed into a benzene-ring structure. This ideal 2D solid has thus been widely used to describe properties of many carbon-based materials, including graphite (where a large number of graphene sheets are stacked), nanotubes (where graphene sheets are rolled up into nanometer-sized cylinders), large fullerenes (where graphene sheets contain at least 12 pentagons displaying a spherical shape), and ribbons (where graphene is cut into strips). Planar graphene itself was presumed not to exist in the free state, being unstable with respect to the for-

mation of curved structures, such as soot, fullerenes, and nanotubes.

However, a couple of years ago, researchers went on to actually prepare graphene by mechanical exfoliation (repeated peeling or micromechanical cleavage) of bulk graphite (highly oriented pyrolytic graphite: HOPG) [1,2] or by epitaxial growth through thermal decomposition of SiC [3]. Such a discovery of a simple method to transfer a single atomic layer of carbon from the c-face of graphite to a substrate suitable for the measurement of its electrical properties has led to a renewed interest in what was considered to be a prototypical, yet theoretical, two dimensional system. Graphene displays, indeed, unusual electronic properties arising from the confinement of electrons in two dimensions and peculiar geometrical symmetries. Indeed, old theoretical studies of graphene [4,5] reveal that the specific linear electronic band dispersion near the Brillouin zone corners (Dirac point) gives rise to electrons and holes that propagate as if they were massless Fermions, with a velocity on the order of one hundredth of the velocity of light. Charge excitations close to the Fermi level can thus be formally described as massless relativistic particles obeying a Dirac equation, whereas a new degree of freedom reflecting inherent symmetries (sublattice degeneracy) appears in the electronic states: the pseudospin. Because of the resulting pseudospin symmetry, electronic

a e-mail: jean-christophe.charlier@uclouvain.be
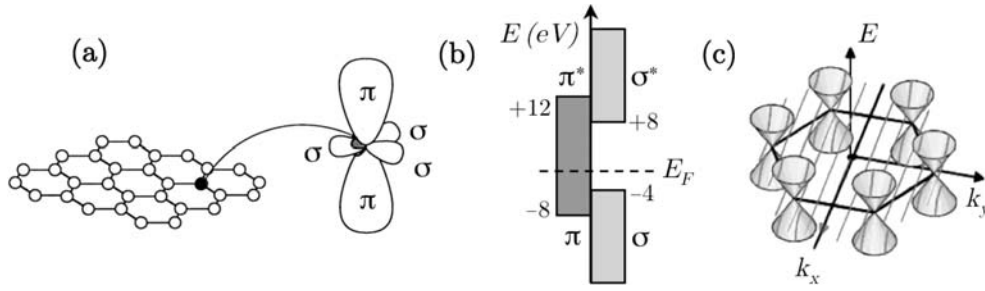
Fig. 1. Illustration of the carbon valence orbitals (a): the three σ orbitals in graphene and the π orbital perpendicular to the sheet. The σ bonds in the carbon hexagonal network strongly connect the carbon atoms and are responsible for the binding energy and the elastic properties of the graphene sheet. The π bonds are perpendicular to the surface of the sheet. The corresponding bonding and the anti-bonding σ bands are separated by a large energy gap of $\sim$12 eV (b), while the bonding and anti-bonding π states lie in the vicinity of the Fermi level (E_F). Consequently, the σ bonds are frequently neglected for the prediction of the electronic properties of graphene around the Fermi energy.

states turn out to be particularly insensitive to external sources of elastic disorder (topological and electrostatic defects) and, as a result, charge mobilities in graphene layers as large as 10^5 cm^2 V^{-1} s^{-1} have been reported close to the Dirac point [1]. In addition, in suspended graphene, the minimum conductivity at the Dirac point approaches a universal (geometry independent) value of $4e^2/\pi h$ at low temperature [7]. Low temperature electron mobility approaching 2×10^5 cm^2 V^{-1} s^{-1} were measured for carrier density below 5×10^9 cm^{-2}. Such values cannot be attained in conventional semiconductors. In addition, graphene has been shown to exhibit anomalous quantum transport properties such as an anomalous integer quantum Hall effect [8,9], but also one of the most exotic and counterintuitive consequences of quantum electrodynamics: the unimpeded penetration of relativistic particles through high and wide potential barriers, known as the Klein paradox [10]. These discoveries have stirred a lot of interest in the scientific community as well as in the international media. The excitement behind this discovery has two main driving forces: basic science and technological implications [11]. Because of its high electronic mobility, structural flexibility, and capability of being tuned from p-type to n-type doping by the application of a gate voltage, graphene is considered a potential breakthrough in terms of carbon-based nano-electronics.

The goal of this paper is thus to review the electronic states of 2D graphene and to understand how these specific properties are conserved or modified in 1D nanostructures such as carbon nanotubes and graphene nanoribbons. In the following, the first section is devoted to an overview of the electronic properties of graphene using a simple nearest neighbor tight-binding model. A description of how ab initio calculations modify this approach is also presented. In the second part, quasi-1D structures, known as graphene nano-ribbons (GNRs), are illustrated, focusing on the appearance of energy gaps that increase with the width reduction, opening the possibility for bandgap engineering through confinement effects. These GNRs structures turn out to share some strong geometrical similarities with carbon nanotubes (CNTs), often viewed as resulting from a rolling up procedure from

a graphene ribbon, as presented in Section 3. Carbon nanotubes (CNTs) are shown to exist in two flavors, respectively metallic or semiconducting depending on their helical symmetry. Metallic tubes usually display exceptionally large mean free path and very low resistance close to the theoretical limit of the quantum resistance (h/e^2), because of pseudospin symmetry and poor efficiency of elastic backscattering. Semiconducting tubes show an energy gap downscaling with their diameter.

Chemical doping and defects in graphene based materials are currently being actively explored as a potential source of innovation to taylor the electronic properties of these nanostructures. Such novel class of hybrid carbon-based nanomaterials are thus available either to study quantum charge transport phenomena in complex systems, or to engineer novel functions to improve or complement the silicon-based CMOS technologies. Their properties remain to be fully characterized through proper experimental techniques and simulations tools which should play a key role in their unambiguous prediction.

2 Electronic properties of graphene

Graphene is the ideal bidimensional (2D) allotropic form of carbon where the atoms are periodically arranged in an infinite hexagonal network (Fig. 1a). Such an atomic structure is characterized by two types of bonds and exhibits the so-called planar sp^2 hybridization. Indeed, among the four valence orbitals of the carbon atom (the $2s$, $2p_x$, $2p_y$ and $2p_z$ orbitals, where $\vec{z}$ is perpendicular to the sheet), the (s, p_x, p_y) orbitals combine to form the in-plane σ (bonding or occupied) and σ^* (anti-bonding or unoccupied) orbitals. Such orbitals are even with respect to the planar symmetry. The σ bonds are strong covalent bonds responsible for most of the binding energy and for the elastic properties of the graphene sheet (Fig. 1a). The remaining p_z orbital, pointing out of the graphene sheet (Fig. 1a), is odd with respect to the planar symmetry and cannot couple with the σ states. The lateral interaction with neighboring p_z orbitals (labeled the $pp\pi$ interaction) creates the delocalized π (bonding) and π^* (anti-bonding)
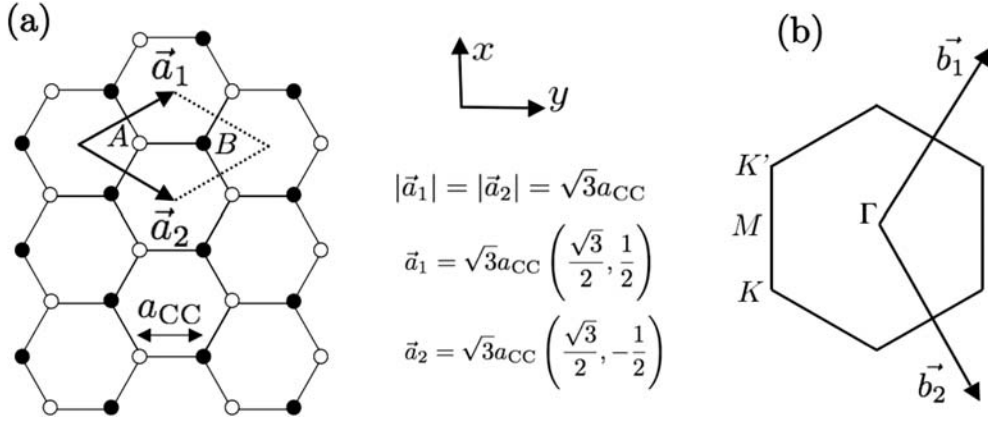
Fig. 2. Basis vectors in the hexagonal lattice of graphene (a) and the corresponding Brillouin zone (b). The reciprocal basis vectors read: $\vec{b}_1 = b(1/2, \sqrt{3}/2)$ and $\vec{b}_2 = b(1/2, -\sqrt{3}/2)$, with $b = 4\pi/a\sqrt{3}$ where $a = \sqrt{3}a_{CC}$ and $a_{CC} = 1.42$ Å is the carbon-carbon distance in graphene.

orbitals [4]. Graphite is comprised of coherently stacked layers of graphene. Two layers are needed to define the unit cell in graphite since the two sheets are translated from each other by a C–C distance ($a_{CC} = 1.42$ Å). The three-dimensional structure of graphite is therefore held together by weak interlayer van der Waals forces including some electronic delocalization [12]. These π bonds, perpendicular to the graphene sheet, are responsible for this weak interaction between carbon layers in graphite.

The electronic structure of graphene can be described using a rather simple tight-binding Hamiltonian, leading to analytical solutions for their energy dispersion and related eigenstates [13]. Since the bonding and anti-bonding σ bands are well separated in energy (>12 eV at Γ), they are frequently neglected in semi-empirical calculations as they are too far away from the Fermi level to play a role (Fig. 1b). Only the remaining two π bands are thus needed to describe the electronic properties of graphene [4] and graphite [5]. Indeed, the bonding π- and anti-bonding carbon π^*-orbitals do form wide electronic valence and conduction bands (Fig. 1b) which cross the Fermi level at high-symmetry points in the Brillouin zone of graphene, as briefly discussed in the following.

The graphene plane is an hexagonal lattice with two atoms per unit cell (A and B) and a basis defined by the vectors $(\vec{a}_1, \vec{a}_2)$ (Fig. 2a). The underlying symmetry of graphene and the presence of these two A–B sublattices will have strong influence on the transport properties of this 2D system. The condition $\vec{a}_i \cdot \vec{b}_j = 2\pi\delta_{ij}$ allows one to obtain the reciprocal lattice vectors $(\vec{b}_1, \vec{b}_2)$ (Fig. 2b). When the atoms are placed onto the graphene hexagonal lattice (Fig. 2a), the electronic wavefunctions from different atoms overlap. However, such an overlap between the p_z orbitals and the s or the p_x and p_y electrons is strictly zero by symmetry. Consequently, the p_z electrons, which form the π bonds in graphene, can be treated independently from the other valence electrons. Within this π-band approximation, the A atom (or B atom) is uniquely defined by one orbital per atom site $p_z(\vec{r} - \vec{r}_A)$ (or $p_z(\vec{r} - \vec{r}_B)$).

To derive the electronic spectrum of the total Hamiltonian, the corresponding Schrödinger equation has to be solved, and by applying the Bloch theorem, the wavefunctions can be written as follows:

$$\Psi(\vec{k}, \vec{r}) = c_A(\vec{k})\tilde{p}_z^A(\vec{k}, \vec{r}) + c_B(\vec{k})\tilde{p}_z^B(\vec{k}, \vec{r}) \tag{1}$$

with

$$\tilde{p}_z^A(\vec{k}, \vec{r}) = \frac{1}{\sqrt{N_{cells}}} \sum_{\vec{\ell}} e^{i\vec{k}.\vec{\ell}} p_z(\vec{r} - \vec{r}_A - \vec{\ell}) \tag{2}$$

$$\tilde{p}_z^B(\vec{k}, \vec{r}) = \frac{1}{\sqrt{N_{cells}}} \sum_{\vec{\ell}} e^{i\vec{k}.\vec{\ell}} p_z(\vec{r} - \vec{r}_B - \vec{\ell}) \tag{3}$$

where $\vec{k}$ is the electron momentum, N_{cells} the number of unit cells in the graphene sheet, and $\vec{\ell}$ the cell position index. The spectrum is derived by solving the Schrödinger equation that reduces to a 2×2 matrix diagonalization:

$$\begin{pmatrix} \mathcal{H}_{AA} - E & \mathcal{H}_{AB} \\ \mathcal{H}_{BA} & \mathcal{H}_{BB} - E \end{pmatrix} \tag{4}$$

where the matrix elements are defined as:

$$\mathcal{H}_{AA}(\vec{k}) = \frac{1}{N_{cells}} \sum_{\vec{\ell},\vec{\ell'}} e^{i\vec{k}.(\vec{\ell'}-\vec{\ell})} \langle p_z^{A,\vec{\ell}} \mid \mathcal{H} \mid p_z^{A,\vec{\ell'}} \rangle \tag{5}$$

$$\mathcal{H}_{AB}(\vec{k}) = \frac{1}{N_{cells}} \sum_{\vec{\ell},\vec{\ell'}} e^{i\vec{k}.(\vec{\ell'}-\vec{\ell})} \langle p_z^{A,\vec{\ell}} \mid \mathcal{H} \mid p_z^{B,\vec{\ell'}} \rangle \tag{6}$$

with the notation: $p_z^{A,\vec{\tau}} = p_z(\vec{r} - \vec{r}_A - \vec{\tau})$ and $p_z^{B,\vec{\tau}} = p_z(\vec{r} - \vec{r}_B - \vec{\tau})$. Here, the overlap matrix elements S have been neglected, where $S = \langle \tilde{p}_z^A | \tilde{p}_z^B \rangle$ between neighboring $\tilde{p}_z$ orbitals (neglect of overlap integrals defines the so-called orthogonal tight-binding schemes). After simple manipulations, and by restricting the interactions to first-nearest-neighbors only, one gets:

$$\mathcal{H}_{AB}(\vec{k}) = \langle p_z^{A,0}|\mathcal{H}|p_z^{B,0}\rangle + e^{-i\vec{k}.\vec{a}_1} \langle p_z^{A,0}|\mathcal{H}|p_z^{B,-\vec{a}_1}\rangle$$

$$+ e^{-i\vec{k}.\vec{a}_2} \langle p_z^{A,0}|\mathcal{H}|p_z^{B,-\vec{a}_2}\rangle = -\gamma_0\alpha(\vec{k}) \tag{7}$$
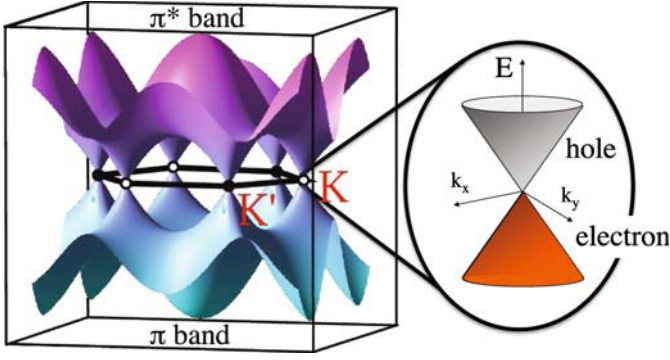
Fig. 3. Graphene π and π^* electronic bands. In this simple approach, the π and π^* bands are symmetric with respect to the valence and conduction bands. Linear dispersion relation close to the K (white dots) and K' (black dots) points of the first 2D Brillouin zone are illustrated using the Dirac cone.

with γ_0 the transfer integral between first neighbors π orbitals (typical values for γ_0 are 2.9–3.1 eV, Ref. [5,14]), $\alpha(\mathbf{k}) = (1 + e^{-i\mathbf{k}.\mathbf{a}_1} + e^{-i\mathbf{k}.\mathbf{a}_2})$ and $\langle p_z^{A,0}|\mathcal{H}|p_z^{A,0}\rangle = \langle p_z^{B,0}|\mathcal{H}|p_z^{B,0}\rangle = 0$ as the energy reference. The dispersion relations are then readily obtained:

$$E^{\pm}(\vec{k}) = \pm\gamma_0$$
$$\times \sqrt{3 + 2\cos(\vec{k}.\vec{a}_1) + 2\cos(\vec{k}.\vec{a}_2) + 2\cos(\vec{k}.(\vec{a}_2 - \vec{a}_1))} \quad (8)$$

which can be further developed as

$$E^{\pm}(k_x, k_y) = \pm\gamma_0$$
$$\times \sqrt{1 + 4\cos\frac{\sqrt{3}k_x a}{2}\cos\frac{k_y a}{2} + 4\cos^2\frac{k_y a}{2}} \quad (9)$$

by setting $a = \sqrt{3}a_{CC}$ ($a_{CC} = 1.42$ Å is the carbon-carbon distance in graphene). The $\vec{k} = (k_x, k_y)$ vectors that belong to the first hexagonal Brillouin zone (BZ) constitute the ensemble of available electronic momentum.

With one p_z electron per atom in the $\pi - \pi^*$ model (the three other s, p_x, p_y electrons fill the low-lying σ band), the $(-)$ band (negative energy branch) in equation (9) is fully occupied, while the $(+)$ branch is empty. These occupied and unoccupied bands cross at the K or K' points which are connected by time reversal symmetry. It is easy to verify that $\alpha(\vec{k} = K) = \alpha(\vec{k} = K') = 0$. The Fermi level E_F (or charge neutrality point) is therefore the zero-energy reference in Figure 3 and the Fermi surface is defined by the set of K and K' points. Since occupied and unoccupied bands do cross, the graphene sheet displays a metallic (zero gap) character. However, as the Fermi surface is of zero dimension (since it is reduced to a discrete and finite set of points), the term semimetal with no overlap or zero-gap semiconductor is usually used. In addition, the π-band electronic dispersion for graphene near these six corners of the 2D hexagonal Brillouin zone is found to be linear. The electronic properties of graphene can thus be described by an effective massless Dirac fermion model

in the vicinity of the charge neutrality point, with linear dispersion and electron-hole symmetry. These "Dirac cones" of carriers (holes and electrons) appear in the corners of the 2D Brillouin zone whose points touch at the Fermi energy, as illustrated in Figure 3. The six points where the Dirac cones touch are referred to as the Dirac points.

This simple orthogonal tight-binding model [4] yields π and π^* zone-center Γ energies which are symmetric ($\pm\gamma_0$) with respect to E_F. In fact, the anti-bonding (unoccupied) π^* bands are located at an higher energy if the overlap integral S is not set to zero (as illustrated in Fig. 1b). A better (but more complicated) $\pi-\pi^*$ parametrization, could lead to analogous results [15], as well as in the case of more accurate first-principles calculations.

In the present paper, the ab initio ground-state properties of graphene (as well as for the nanotubes and the graphene nanoribbons in the following sections) are investigated using the density functional theory (DFT) [16,17] as implemented both in the ABINIT [18] and the SIESTA codes [19]. Using the outlined DFT formalisms, ab initio ground state calculations are performed within the local density approximation. Periodic boundary conditions are used to insure at least 10 Å of vacuum between graphene planes, nanotubes and ribbons in neighboring cells. When dealing with a large number of carbon atoms in the nanostructure supercell, numerical atomic orbital basis sets (double-ζ plus one polarization) are used rather than plane-waves to expand the wave-functions, in conjunction with norm-conserving pseudo-potentials [20]. The energy levels are populated using a Fermi-Dirac distribution with an electronic temperature of 300 K. The integration over the 1D Brillouin zone is replaced by a summation over a regular grid of k-points (between 10–40) in the graphene plane or along the nanostructure axis. The geometry is fully relaxed until the forces on each atom and on the unit cell are less than 0.01 eV/Å and 0.05 eV/Å, respectively.

The ab initio electronic bands of graphene [13] along the high-symmetry M–Γ–K directions are presented in Figure 4. Its space group ($P3m$) contains a mirror symmetry plane, allowing symmetric σ and anti-symmetric π states to be distinguishable. In a 2D crystal, a parallel mirror symmetry operation separates the eigenstates for the whole Brillouin zone, and not only along some high-symmetry axis. The π and π^* bands cross at the vertices of the hexagonal Brillouin zone (vertices labeled by their momentum vector usually denoted by K and K' as mentioned above). Ab initio calculations confirm that the π and π^* bands are quasi-linear (linear very close to K or K' and near the Fermi energy), in contrast with the quadratic energy-momentum relation obeyed by electrons at band edges in conventional semiconductors. When several interacting graphene planes are stacked as in few-layer graphite (nGLs) or in the perfect graphite crystal, the former anti-symmetric π bands are split (owing to bonding or anti-bonding patterns), whereas the σ bands are much less affected by the stacking, as explained in the following sections.
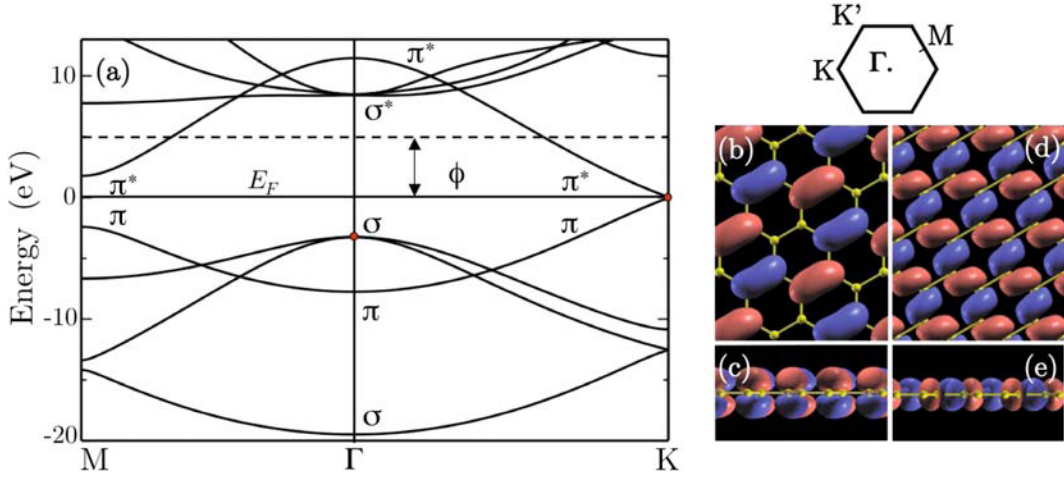
Fig. 4. (a) Electronic band structure of graphene. The bonding σ and the anti-bonding σ^* bands are separated by a large energy gap. The bonding π (highest valence band) and the anti-bonding π^* (lowest conduction band) cross at the K points of the Brillouin zone. The Fermi energy (E_F) is set to zero and ϕ indicates the work function. Above the vacuum level (dotted horizontal line), the states of the continuum are difficult to describe and merge with the σ^* bands. The 2D hexagonal Brillouin zone is illustrated with the high-symmetry points Γ, M, and K (or K'). (b, c) π state at K and (d, e) σ-state at Γ, seen respectively from above and from the side of the graphene plane. Note that the π wavefunction cancels on an hexagonal sublattice due to the $e^{iK\cdot r}$ phase factor. The π (σ) state is odd (even) with respect to the graphene plane reflection.

Graphene is thus highly specific for this linear energy-momentum relation, leading to *massless* fermions. Their electronic group velocities, estimated at the Dirac point, is quite high: $\sim 8.5 \times 10^5$ m/s. Indeed, expanding equation (9) at K (or K') yields the linear π and π^* bands for the Dirac fermions:

$$E^{\pm}(\kappa) = \pm \hbar v_F |\kappa| \qquad (10)$$

where $\kappa = k - K$, and $v_F = \sqrt{3}\gamma_0 a/2\hbar$ is the electronic group velocity. Consequently, graphene exhibits electronic properties that are distinctive for a 2D gas of particles described by the relativistic Dirac equation rather than the non-relativistic Schrödinger equation (only valid for non-relativistic electrons with a finite mass). Indeed, in graphene, charge carriers mimic relativistic particles with zero mass and an effective "speed of light" $c^* \sim 10^6$ m/s.

The linear dispersion given by equation (10) is the solution to the following effective Hamiltonian at the K (or K') point:

$$H = \hbar v_F (\sigma \kappa) \qquad (11)$$

where $\kappa = -i\nabla$ and σ's are the pseudospin Pauli matrices operating in the space of the electron amplitude on the A–B sublattices of graphene. Several unusual transport properties of graphene derived from the linear dispersion and the chiral nature of the quasiparticles defined by equations (10) and (11).

Transport measurements are mostly performed on single-layer graphene field effect transistor (FET) as a function of gate voltage [9]. Graphene FETs are fabricated with standard lithography and etching techniques using mechanically cleaved graphene flakes [2]. A degenerately doped silicon substrate serves as a gate and continuously tunes the 2D carrier density n_s across the Dirac point from hole type to electron type, covering a range of roughly $\pm 1 \times 10^{13}/\text{cm}^2$. Resistivity measurements performed on a single-layer graphene FET reveal that the conduction is symmetric about the Dirac point [21]. In the high-density regime, the mobility is roughly carrier density-independent and temperature-independent. Reported mobility values range from 2000 to 20 000 cm^2/V s, with the high end representing a long mean free path of $\sim 0.3~\mu$m, comparable to that of single-wall carbon nanotubes (as described in the following sections). Its weak temperature dependence indicates impurity or defect scattering as the dominant mobility-limiting mechanism and provides room for future improvement. Possible sources of scattering include adsorbents and defects in the graphene lattice and ionized impurities in the SiO$_2$ substrate. In addition, transport measurements also reveal a remarkable property of 2D carriers in graphene. Although the carrier density approaches zero at the Dirac point, the 2D resistivity ρ_{xx} or conductivity σ_{xx} remains finite. Such behavior, dubbed "minimum" conductivity, has been observed in many devices with ρ_{xx} ranging from 2–7 $k\Omega$ [8,9]. Slightly larger values of ρ_{xx} from 6–9 kΩ are also reported for bi-layer graphene [22]. The origin of this unusual behavior remains unclear at the moment. Extrinsic mechanisms, such as density inhomogeneity caused by ionized impurities in the SiO$_2$ substrate or by the rippling of the graphene sheet [23], may lead to a finite conductivity [24]. However, a minimum quantum conductivity can also arise intrinsically from the linear excitation spectrum of Dirac fermions and/or the chirality of the quasiparticles [11].

Despite a conductivity that never falls below a minimum value (e^2/h) even when the carrier concentrations tend to zero, graphene has also revealed other unusual transport phenomena characteristic of two-dimensional Dirac fermions, such as an anomalous integer quantum
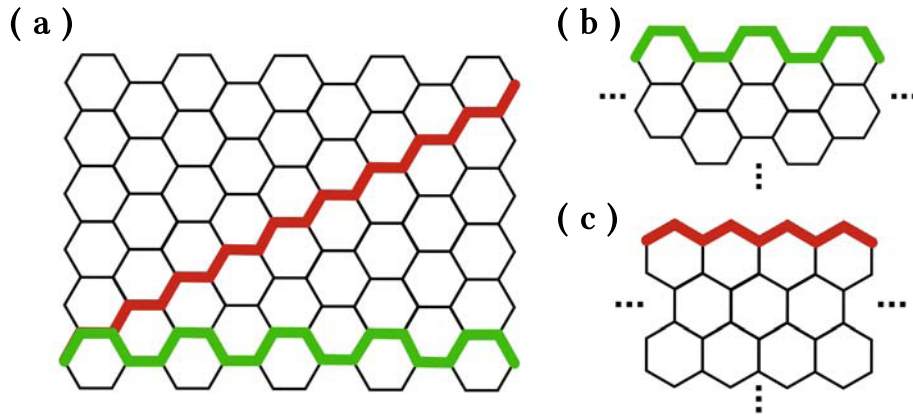
Fig. 5. Honeycomb lattice of graphene (a) with both the *zigzag* (red) and the *armchair* (green) directions. Graphene nanoribbons cut in the ideal sheet along these two highly symmetric directions are called aGNRs (b) and zGNRs (c), respectively.

Hall effect, a cyclotron mass m of massless carriers with an energy E in graphene that is described by $E = mc^{*2}$, and Shubnikov-de Haas oscillations in graphene which exhibit a phase shift of π due to Berry's phase [8,9]. However, the accurate description of these unusual transport phenomena exceeds the scope of the present paper and could be find in reference [25].

In this section, the electronic properties of the 2D graphene have been described by an effective massless Dirac fermion model in the vicinity of the charge neutrality point, with linear dispersion and electron-hole symmetry. In the next sections, confinement effects will be described when the graphene sheet is cut in strips like for graphene nanoribbons or rolled up in cylinders such as carbon nanotubes. The remarkable properties of graphene derived close to the K and K' points are found to remain valid for 1-D systems such as metallic nanotubes and wide armchair nanoribbons. However, other symmetries result in semiconducting systems with varying gaps. Semiconducting nanotubes and ribbons with increasing diameter (or width) show a linear downscaling of their associated energy gaps. By using proper boundary conditions, the electronic band structure of both types of systems can be analytically derived. Consequences on the quantum transport of both 1-D systems is also explicitly described.

3 Electronic properties of graphene nanoribbons

High electron mobility and long coherence length make graphene a subject of great interest for nanoscale electronic applications, even for the realization of room-temperature ballistic (dissipation-free) electronics. However, a major setback in the development of graphene-based field-effect transistors is the inability to electrostatically confine electrons in graphene, because a single layer of graphite remains metallic even at the charge neutrality point. In order to overcome this problem, a way to open a gap in the electronic structure of graphene has to be found. A straightforward solution is to pattern the graphene sheet into narrow ribbons. Thanks to recent progresses in preparing single graphite layers on conventional device setups, graphene nanoribbons (GNRs) with varying widths have been synthesized and characterized experimentally [6,26,27].

Graphene nanoribbons (GNRs) are elongated strips of graphene with a finite width that can be obtained by cutting a graphene sheet along a certain direction. Due to the honeycomb structure of graphene, two prototypical shapes are possible for the edges, namely the armchair edge (Fig. 5b) and the zigzag edge (Fig. 5c), with a difference of 30 deg between the two edge orientations. Depending on the cutting direction, the edges of the GNRs may thus exhibit either one of these two "ideal" shapes or more complex geometries composed of a mixture of armchair and zigzag shaped fragments.

The atomic structure of nanoribbons with armchair and zigzag edges is further illustrated in Figure 6 along with their corresponding unit cells. Following previous convention [28–39], GNRs with armchair (zigzag) edges on both sides are classified by the number of dimer lines (zigzag lines) across the ribbon width, as illustrated in Figure 6. In the following, N-aGNR and N-zGNR will refer to such prototypical armchair and zigzag GNRs, N being respectively the number of dimer and zigzag lines. In addition, if not otherwise stated, the dangling bonds on the edge sites of GNRs will be assumed to be terminated by hydrogen atoms, although dangling bonds would not make any contribution to the electronic states near the Fermi level. Of course, these ideally shaped edges does not correspond to the experimental observations [40–42] where GNRs currently have a high degree of roughness at the edges. Some aspect of this edge disorder will be presented later on.

The presence of the edges in GNRs entails the quantum mechanical constriction of electronic wavefunctions in the direction perpendicular to the axis of the ribbon and, as a consequence, a confinement-induced gap can open. Since GNRs are just geometrically terminated single graphite layers, their electronic structures have been modeled by imposing appropriate boundary conditions

(a)   (b)

1   2   3   4   N-1 N   1 2 3 4   N-1 N
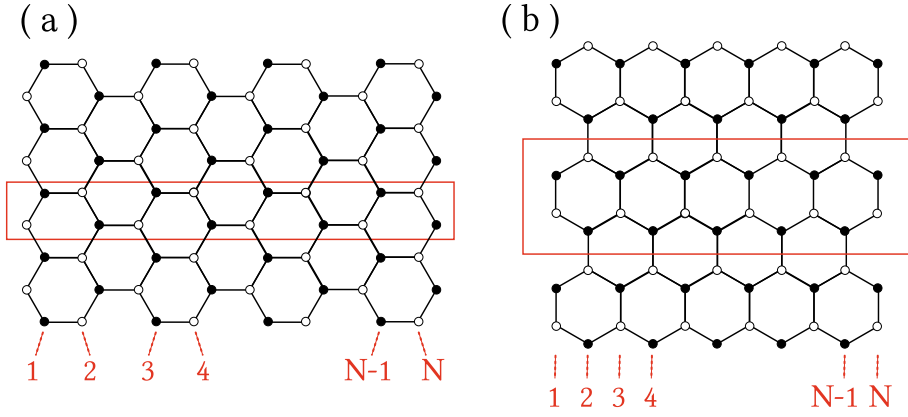
Fig. 6. Carbon N-zGNR (a) and N-aGNR (b) composed of N armchair and zigzag lines, respectively. Black and white dots identify carbon atoms belonging to the two different graphene sublattices (A and B). The red rectangle represents the 1D unit-cell of the corresponding GNR. Atoms labeling follows the counting of zigzag chains (a) or dimer lines (left), from 1, 2, 3, 4, ... to N-1, N.

(a)   (b)
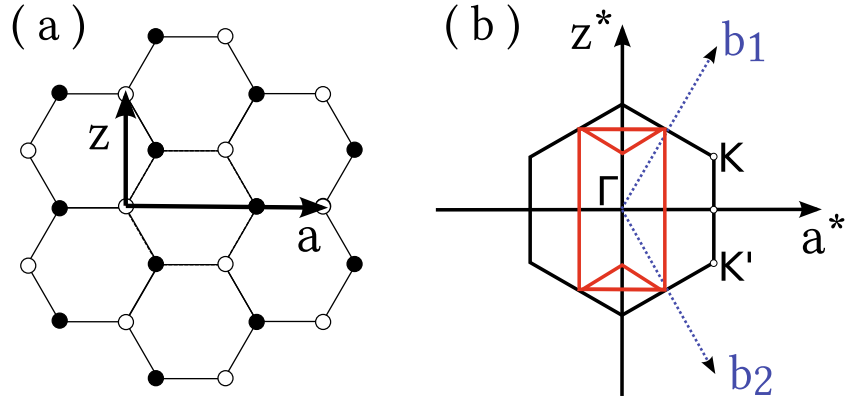
Fig. 7. Band folding approximation. (a) Honeycomb network of graphene with the two directions of the electronic confinement (a and z black arrows) for the zigzag and armchair ribbons, respectively. (b) The first hexagonal Brillouin zone of graphene is folded into the first rectangular Brillouin zone (red), defined by the $a^\star$ and $z^\star$ directions. This rectangular Brillouin zone corresponds in the reciprocal space to the unit cell constructed using the a and z vectors in real space as illustrated in (a).

(insuring the confinement of the electrons within the ribbon) on the Schrödinger's equation within the simple single-band tight-binding approximation based on π-states of graphene [28,29,34] or on the two-dimensional free massless particle Dirac's equation with an effective speed of light ($\sim 10^6$ m/s) [35–37]. This additional quantum confinement of the electrons with respect to the graphene case induces a discretization of the wave vector in the confined direction and breaks the spectrum into subbands for both aGNRs and zGRNs. Figure 7 illustrates the directions of electronic confinement denoted a and z in the real space for the zigzag and armchair ribbons respectively. As pointed out in Figure 7a, taking a rectangular real space unit cell build on the vectors a and z makes the graphene Brillouin zone to fold into the rectangular area constructed on the vectors a^* and z^*. By extension, in the case of large zigzag and armchair GNRs, the graphene Brillouin zone reduces to elongated rectangular stripes aligned with z^* and a^* respectively (Fig. 7b).

Consequently, the energy π-states band spectrum of graphene can be projected along the $a^\star$ and $z^\star$ directions,

thus predicting the π-states band structures of both armchair and zigzag ribbons of sufficiently large width, as depicted in Figure 8. The main result of the present zone folding approximation is that the linear dispersion relation of graphene observed around the Dirac points K and K' is preserved and is predicted to be localized at $k = 0$ and $k = \pm 2\pi/3$ for aGNRs and zGNRs, respectively. In summary, as for 2-D graphene, such a nearest neighbor tight-binding model is found to describe low energy properties with a degree of approximation high enough for many applications and is widely employed for studying transport properties in GNRs [28,45–49].

However, ab initio calculations [38] reveal that GNRs with hydrogen passivated armchair or zigzag shaped edges always have nonzero and direct band gaps, originating from quantum confinement, and edge effects play a crucial role [43,44]. Consequently, although the graphene model based on the π-states of carbon is known to accurately describe the energy dispersion of the carbon sheet, a careful consideration of edge effects in nanometer sized ribbons is required to determine their band gaps because, unlike the
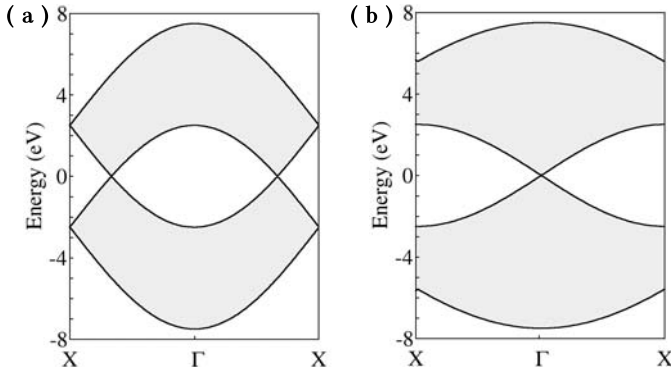
Fig. 8. Energy band structure of graphene projected on the zigzag (a) and armchair (b) axis. The linear dispersion relations are conserved and localized at $k = 0$ for aGNRs and at $k = \pm 2\pi/3$ for zGNRs.

situation in graphene, the bonding characteristics between atoms change abruptly at the edges [31,34]. In the following, a tight-binding derivation of the electronic properties of armchair and zigzag GNRs are described and compared with DFT calculations.

3.1 Electronic properties of armchair nanoribbons (aGNRs)

As predicted in the previous section, the linear dispersion relation of graphene is conserved when projected on the one dimensional Brillouin zone of aGNRs. This simple zone folding approximation provides a correct description of the global shape of the band structure, but additional effects related to the detailed nature of the edges have to be taken into account in order to accurately describe the low energy electronic states. The tight-binding approximation can partly tackle this problem. In analogy with what has been suggested previously for graphene, the tight-binding Hamiltonian of the nanoribbons is constructed as:

$$\mathcal{H} = \sum_i \epsilon_i \hat{c}_i^\dagger \hat{c}_i + \sum_{i,j} \gamma_{ij} \hat{c}_i^\dagger \hat{c}_j \qquad (12)$$

where ϵ_i are the atomic on-site energies, γ_{ij} correspond to the hopping energies, and $\hat{c}_i$ is an operator which creates an electron at site i. In order to simplify the formulation, on-site energies are conventionally set as the reference energy ($\epsilon_i = \epsilon = 0$). Using the restriction of electron hopping only between first-nearest neighbors, the hopping parameters are supposed to be all equal and reduced to $\gamma_{ij} = \gamma_0$. This assumption is equivalent to assume that the ribbon edges are passivated in such a way that bulk graphene is reproduced.

Taking into account the periodicity along the axis of the aGNRs, the tight-binding Hamiltonian of the armchair ribbons can be represented as Bloch sums over the

basis 1A, 1B, 2A, 2B, ... NA, NB as illustrated in Figure 6:

$$\mathcal{H}_k = \gamma_0 \hat{\phi}_k^\dagger \begin{pmatrix} 0 & e^{ik\frac{a}{2}} & 0 & 1 & 0 & 0 & \cdots \\ e^{-ik\frac{a}{2}} & 0 & 1 & 0 & 0 & 0 & \cdots \\ 0 & 1 & 0 & e^{ik\frac{a}{2}} & 0 & 1 & \cdots \\ 1 & 0 & e^{-ik\frac{a}{2}} & 0 & 1 & 0 & \cdots \\ 0 & 0 & 0 & 1 & 0 & e^{ik\frac{a}{2}} \cdots \\ 0 & 0 & 1 & 0 & e^{-ik\frac{a}{2}} & 0 & \cdots \\ \cdots & \cdots & \cdots & \cdots & \cdots & \cdots & \cdots \end{pmatrix} \hat{\phi}_k$$

$$(13)$$

where $\hat{\phi}_k = (\hat{c}_k(1A), \hat{c}_k(1B), \hat{c}_k(2A), \hat{c}_k(2B), \ldots, \hat{c}_k(NA), \hat{c}_k(NB))$.

The energy band structures of armchair ribbons are calculated by diagonalizing the Hamiltonian of equation (13) and illustrated in Figure 9 for two different ribbon widths. In agreement with the prediction of the band-folding approximation, the typical Dirac-like linear dispersion or the direct gap always appears at $k = 0$.

Interestingly, the calculated band structures highlight the crucial role of the ribbon width upon the energy gap. While two third of the ribbons appear to exhibit a semiconducting behavior, the last third is found to remain metallic. Indeed, such a simple calculation can be repeated for several ribbon widths, revealing that the gap of the ribbon presents an oscillating behavior with respect to N with a period of 3. In fact, at $k = 0$, the eigenvalues of the tight-binding Hamiltonian can be extracted analytically [50], leading to an energy gap (Δ_N) which is width dependent:

$$\Delta_N = \begin{cases} \Delta_{3\ell} & = |\gamma_0| \left(4\cos\frac{\pi\ell}{3\ell+1} - 2 \right) \\ \Delta_{3\ell+1} = |\gamma_0| \left(2 - 4\cos\frac{\pi(\ell+1)}{3\ell+2} \right) \\ \Delta_{3\ell+2} = 0 \end{cases} \qquad (14)$$

with $\Delta_{3\ell} > \Delta_{3\ell+1} > \Delta_{3\ell+2} = 0$.

As a consequence, the present tight-binding approach predicts that N-aGNRs are metallic for every $N = 3\ell + 2$ (where ℓ is a positive integer), and semiconducting in the other cases. When compared with ab initio calculations, this simple TB model with one orbital per site and constant hopping energy between nearest neighbors appears to accurately describe the band structure of the armchair ribbons. However, DFT calculations reveal that even for the $3\ell + 2$-GNRs (predicted to be metallic in TB) a small gap opens at $k = 0$ inducing a semiconductor character for all armchair ribbons [38,39]. The energy gaps decrease as the widths of the aGNR increase, reaching the zero-gap value of graphene for infinite ribbon width. For a ribbon of $\sim$5 nm with a metallic behavior predicted by the tight-binding model, the ab initio estimated band gap is only $\sim$0.05 eV.

To understand the origin of this gap opening, it has to be noted that the prediction of the TB model entirely results from the electronic confinement imposed by the boundary conditions at the ribbon edges. Indeed, the perturbation of the on-site and hopping energy induced by the presence of passivated edges is not taken into account.
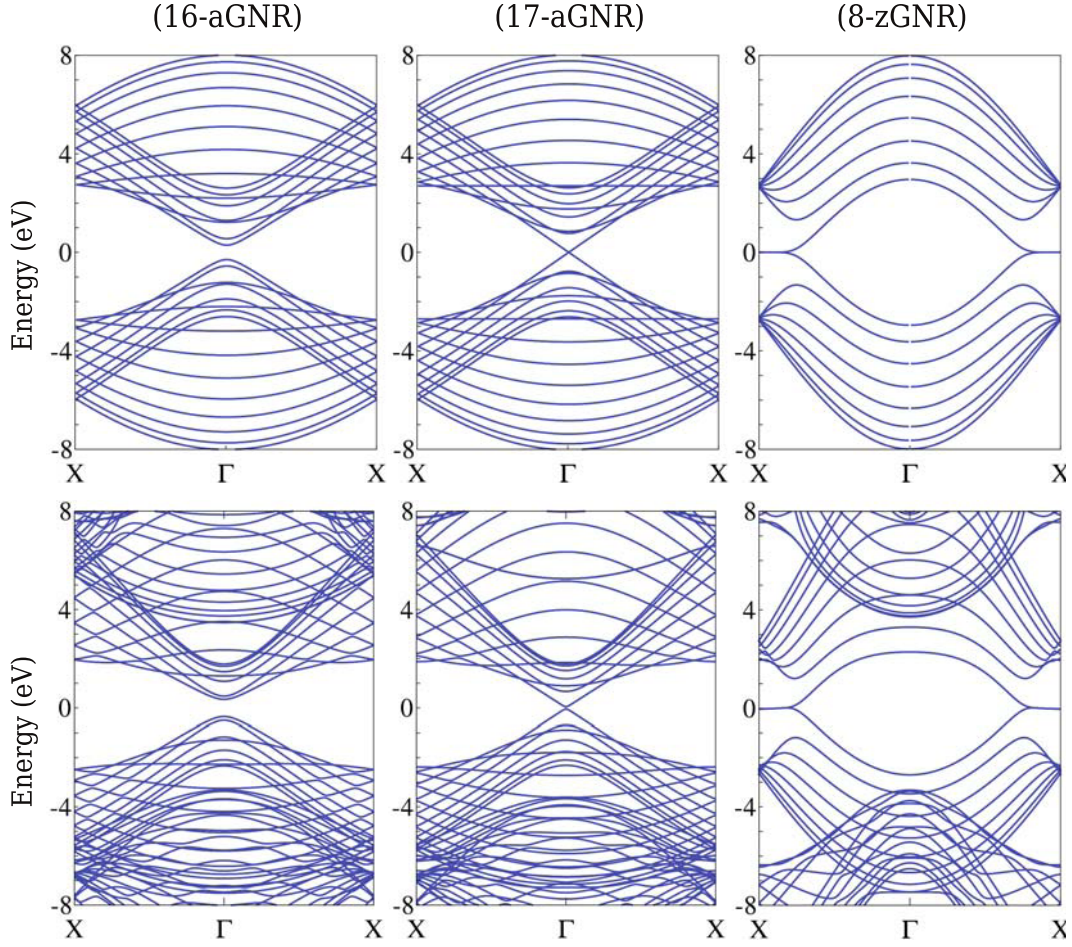
Fig. 9. Energy band structures of two armchair nanoribbons (N-aGNRs) of various width ($N = 16, 17$) and one zigzag nanoribbons (8-zGNR). The tight-binding band structures (top) computed using a constant hopping energy ($\gamma_0 = 2.7$ eV) between nearest neighbors are compared to ab initio band structures (bottom).

However, edge effects are playing a crucial role [38]. Indeed, the edge carbon atoms of the armchair ribbon, are passivated by hydrogen atoms (by some foreign atoms or molecules in general) so that the σ bonds between hydrogen and carbon and the on-site energies of the carbons at the edges would be different from those in the middle of the GNR. The bonding distances between carbon atoms at the edges are also expected to change accordingly, leading to a decrease in interatomic distance from 1.422 Å inducing an increase of $\sim 12\%$ in the hopping integral between π-orbitals, and explaining physically the presence of a band gap for all the aGNRs [38]. The introduction of these modified on-site and hopping energies within a new TB model restricted to nearest neighbors allows to achieve an improved agreement between the TB and DFT band structures, underlying the crucial role of the edges relaxation.

3.2 Electronic properties of zigzag nanoribbons (zGNRs)

For zGNRs, the approach consists in considering explicitly the boundary conditions by imposing that the wavefunc-

tion vanishes at the edges of the ribbon when solving the Dirac equation [35]. As illustrated in Figure 6, one of the zGNR edge is entirely composed of A-type carbon atoms (left one), while the other edge is made up of B-type carbon atoms (right one). Therefore, the boundary conditions can be imposed on the two sublattices separately, leading the wavefunction of the A-type sublattice to vanish on the opposite B-type edge and vice versa. The corresponding tight-binding Hamiltonian may also be expressed as Bloch sums:

$$
\mathcal{H}_k = \gamma_0 \hat{\phi}_k^\dagger
$$
$$
\times \begin{pmatrix}
0 & 2\cos(\frac{ka}{2}) & 0 & 0 & 0 & \cdots \\
2\cos(\frac{ka}{2}) & 0 & 1 & 0 & 0 & \cdots \\
0 & 1 & 0 & 2\cos(\frac{ka}{2}) & 0 & \cdots \\
0 & 0 & 2\cos(\frac{ka}{2}) & 0 & 1 & \cdots \\
0 & 0 & 0 & 1 & 0 & \cdots \\
\cdots & \cdots & \cdots & \cdots & \cdots & \cdots
\end{pmatrix} \hat{\phi}_k
$$

(15)

where $\hat{\phi}_k = (\hat{c}_k(1A), \hat{c}_k(1B), \hat{c}_k(2A), \hat{c}_k(2B), \ldots, \hat{c}_k(NA), \hat{c}_k(NB))$.
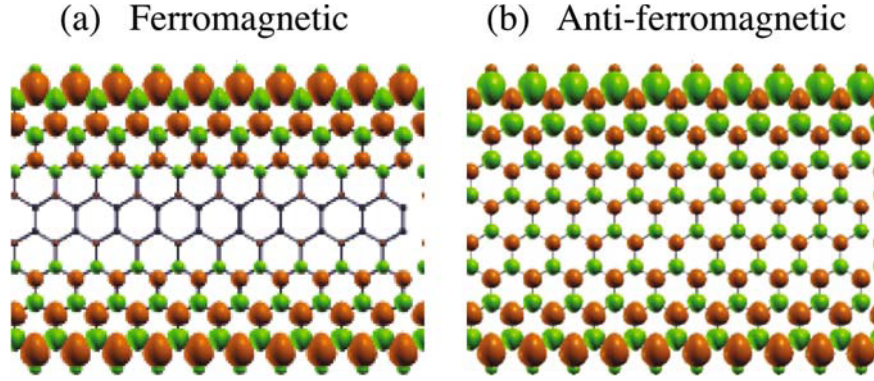
Fig. 10. Spin polarized electronic densities (difference of electronic densities for majority and minority e$^-$) iso-surfaces for the ferromagnetic (a) and anti-ferromagnetic (b) configurations of a 8-zGNR. Red and green surfaces correspond to an excess of majority and minority spin, respectively.

The energy band structures of zigzag ribbons are calculated by diagonalizing the Hamiltonian of equation (15) and illustrated in Figure 9. In agreement with the prediction of the band-folding approximation, the direct gap always appears at $k = \pm 2\pi/3$. Another peculiar feature appears for zGNRs, independently of the ribbon width: the highest valence and lowest conduction bands form two partially flat degenerate bands with zero energy between the Dirac points and the border of the Brillouin zone ($2\pi/3 \leq |k| \leq \pi$), thus inducing a sharp peak in the density of states at E_F. Ab initio computed local densities of states around the Fermi level reveal that these electronic states are mainly located at the zigzag edges of the GNR, and penetrates progressively into the ribbon for wavevectors going from π to $2\pi/3$ inducing these nearly flat bands in Figure 9. Some dispersion appears when the edge states coming from the opposite edges, overlap and form bonding and antibonding states, inducing some amplitude which depends on the ribbon width. Examining the relative importance of the edge state for graphene ribbons with general edges, theory predicts that an edge shape with three or four zigzag sites per sequence is sufficient to show an edge state, the system size being on a nanometer scale [28]. Experimentally, STM and STS measurements [51] also demonstrate that the edge states near the Fermi level are only observed at a zigzag edge and defect points of an armchair edge (and not at a homogeneous one).

Another important feature related to zGNRs consists on the presence of magnetic order (spin degree of freedom) along the zigzag edges. As mentioned above, the zigzag topology induces narrow-band edge states at the Fermi energy allowing possible magnetization at the edges [29,32,33,38,39]. In a magnetic field, these edge states, strongly localized near zigzag edges, generate a rational fraction of the magnetic flux in each hexagon, and thus behave like zero-field edge states [29]. The orbital diamagnetic susceptibility strongly depends on the edge shapes, as the ring currents are very sensitive to the lattice topology near the edge. Because the edge states lead to a sharp peak in the density of states at the Fermi level, zGNRs exhibit a Curie-like temperature dependence of the Pauli paramagnetic susceptibility [29]. Consequently, a crossover is predicted from high-temperature diamagnetic to low-temperature paramagnetic behavior in the magnetic susceptibility in zGNRs [29].

Upon inclusion of the spin degree of freedom, the zGNRs are predicted to have a magnetic insulating ground state with ferromagnetic ordering at each zigzag edge and antiparallel spin orientation between the two edges Figure 10. The difference in total energy per edge atom between non-spin-polarized and spin-polarized edge states is of the order of a few tens of meV [38].

For example, the electronic ground state of the ideal 8-zGNR reveals anti-parallel ($\uparrow\downarrow$) spin orientations between the edges (Fig. 10b) leading to a semiconducting band structure (0.5 eV band gap) with full spin degeneracy. On the other hand, the magnetic configuration with parallel ($\uparrow\uparrow$) spin orientations between the edges (Fig. 10a) is found to be metastable (11 meV/edge-atom higher in energy). This configuration displays a metallic behavior, as the $\pi_\uparrow^*$ and $\pi_\downarrow$ bands are crossing at the Fermi energy, and presents a total magnetic moment of 0.51 μ_B per edge atom.

Consequently, when the spin degree of freedom is taken into account, the presence of energy gaps for electrons in zGNRs can be explained from the staggered sublattice potentials resulting from the magnetic ordering [52]. Such a situation occurs because the opposite spin states on opposite edges occupy different sublattices, respectively. Since the strength of the staggered potentials in the middle of the ribbon decreases as the ribbon width increases, the band gaps of zigzag GNRs are inversely proportional to the width.

In conclusion, the role of the edges is crucial for determining the values and the scaling rule for the band gaps in both armchair and zigzag GNRs. In addition, although the spin-orbit interaction is very small in graphite [53], the coexistence of electrons with opposite spin orientations in 2D graphene, could open a new path to explore spintronics (when the electrical current is completely spin polarized) at the nanometer scale [39].

The next section will be dedicated to the validation of the single-band tight-binding approximation and to the
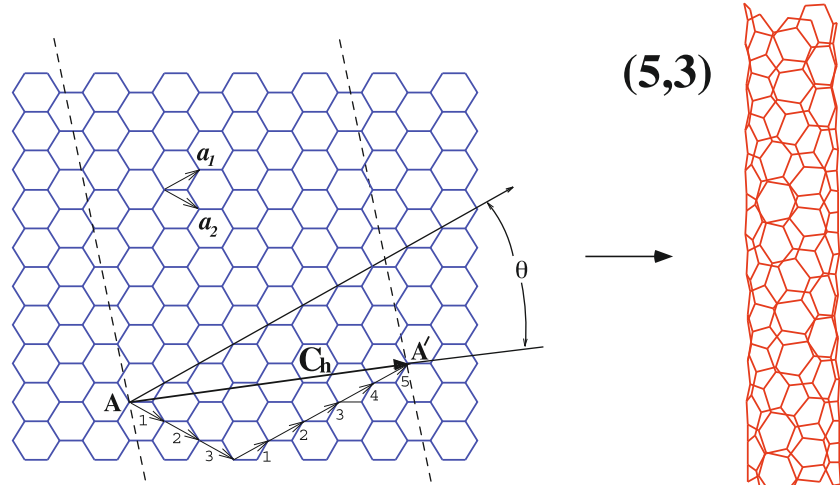
Fig. 11. Graphene honeycomb network in blue with the lattice vectors $\mathbf{a}_1$ and $\mathbf{a}_2$. The chiral vector $\mathbf{C}_h = 5\mathbf{a}_1 + 3\mathbf{a}_2$ represents a possible wrapping of the two-dimensional graphene sheet into a tubular form. The direction perpendicular to $\mathbf{C}_h$ is the tube axis. The chiral angle θ is defined by the $\mathbf{C}_h$ vector and the $\mathbf{a}_1$ "zigzag" direction of the graphene lattice. In the present example, a $(5,3)$ nanotube is under construction and the resulting tube is illustrated in red on the right.

conservation of the corresponding remarkable properties of graphene in carbon nanotubes.

4 Electronic properties of carbon nanotubes

Carbon nanotubes have been discovered and first characterized in 1991 by Iijima from NEC laboratories (Japan) [54]. This discovery was made possible thanks to the use of state-of-the-art transmission microscopy. The firstly-discovered nanotubes were made of several concentric cylindrical-like shells regularly spaced by an amount of about 3.4 Å as in conventional graphite materials. These multiwall nanotubes (MWNTs) were first synthesized with diameter ranging from a few nms to several hundred nms for the inner and outer shells, respectively. As for the length, MWNTs extending over several μms are currently synthesized.

Shortly after the discovery of multiwall carbon nanotubes, singlewall carbon nanotubes (SWNTs) were synthesized in abundance using arc discharge methods with transition metal catalysts [55,56]. A carbon nanotube made of a single graphene layer rolled up into a hollow cylinder is called a singlewall nanotube. These tubes have quite small and uniform diameter, in the order of one nanometer. Such an unprecedented small diameter, combined with the crystalline perfection of the atomic network, explains why such objects were quickly considered as the "ultimate" carbon-based 1D systems.

Since the atomic structure of SWNTs is closely related to that of graphene, the tubes are usually labeled in terms of the graphene lattice vectors. As illustrated in Figure 11, a singlewall carbon nanotube is geometrically obtained by rolling up a single graphene strip [57]. Its structure can be specified or indexed by its circumferential vector ($\mathbf{C}_h$), as defined by the chiral vector (AA' in Fig. 11) which connects two crystallographically equivalent sites (A and A')

on a graphene sheet. In this way, a SWNT's geometry is completely specified by a pair of integers (n,m) denoting the relative position $\mathbf{C}_h = n\mathbf{a}_1 + m\mathbf{a}_2$ of the pair of atoms on a graphene strip which, when rolled onto each other, form a tube ($\mathbf{a}_1$ and $\mathbf{a}_2$ are unit vectors of the hexagonal honeycomb lattice, see Fig. 11).

This chiral vector $\mathbf{C}_h$ defines the circumference of the tube. The diameter of the nanotube can thus be estimated as $d_t = |\mathbf{C}_h|/\pi = \frac{a}{\pi}\sqrt{n^2 + nm + m^2}$, where a is the lattice constant of the honeycomb network ($a = \sqrt{3} \times a_{cc}$ and $a_{cc} \simeq 1.42$ Å the C–C bond length). The chiral vector $\mathbf{C}_h$ uniquely defines a particular (n,m) tube, as well as its chiral angle θ which is the angle between $\mathbf{C}_h$ and $\mathbf{a}_1$ ("zigzag" direction of the graphene sheet, see Fig. 11). The chiral angle θ can be calculated as $\cos\theta = \frac{\mathbf{C}_h \cdot \mathbf{a}_1}{|\mathbf{C}_h||\mathbf{a}_1|} = (2n + m)/(2\sqrt{n^2 + nm + m^2})$. The value of θ is in the range $0 \leq |\theta| \leq 30°$, because of the hexagonal symmetry of the graphene lattice. This chiral angle θ also denotes the tilt angle of the hexagons with respect to the direction of the nanotube axis. Nanotubes of the type $(n,0)$ ($\theta = 0°$) are called *zigzag* tubes, because they exhibit a zigzag pattern along the circumference. Such tubes display carbon-carbon bonds parallel to the nanotube axis. Nanotubes of the type (n,n) ($\theta = 30°$) are called *armchair* tubes, because they exhibit an armchair pattern along the circumference. Such tubes display carbon-carbon bonds perpendicular to the nanotube axis. Both zigzag and armchair nanotubes are achiral tubes, in contrast with general $(n, m \neq n \neq 0)$ chiral tubes (Fig. 12).

The geometry of the graphene lattice and the chiral vector not only determine the diameter of the tube, but also the unit cell, and its number of carbon atoms. The smallest graphene lattice vector $\mathbf{T}$ perpendicular to $\mathbf{C}_h$ defines the translational period t along the tube axis. The lattice vector $\mathbf{T}$ can also be expressed in terms of the basis vectors $\mathbf{a}_1$ and $\mathbf{a}_2$ as $\mathbf{T} = t_1\mathbf{a}_1 + t_2\mathbf{a}_2$, using $\mathbf{C}_h \cdot \mathbf{T} = 0$
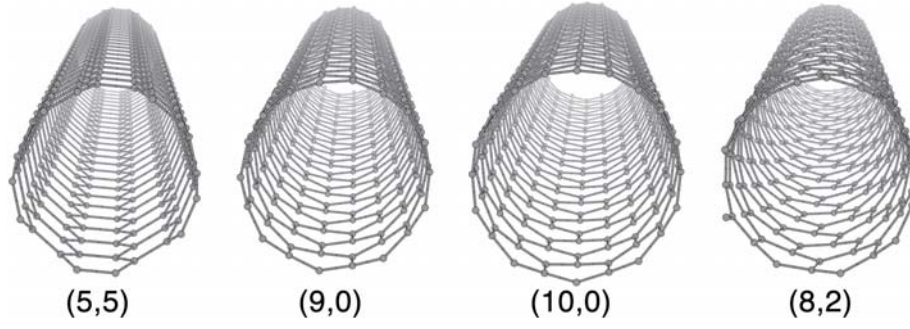
Fig. 12. Atomic structures of $(5,5)$ armchair, $(9,0)$ and $(10,0)$ zigzag, $(8,2)$ chiral nanotubes.
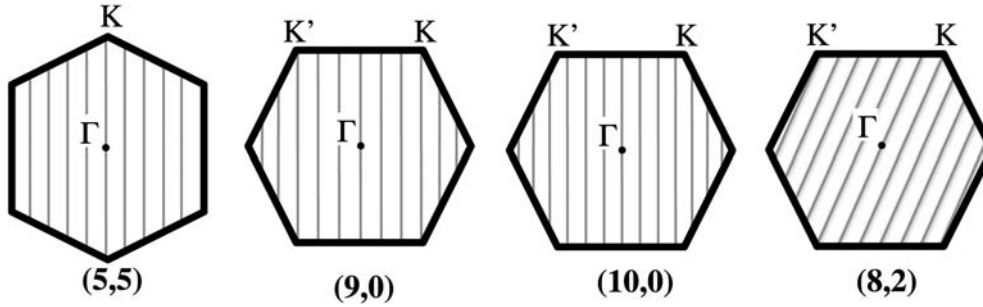
Fig. 13. Allowed **k**-vectors of the (5,5), (9,0), (10,0) and (8,2) tubes mapped onto the graphene Brillouin zone.

and the expressions of $t_1 = (2m + n)/N_R$ and $t_2 = -(2n + m)/N_R$, where N_R is the greatest common divisor of $(2m + n)$ and $(2n + m)$. The length of the translational vector is given by $t = |\mathbf{T}| = \sqrt{3}a\sqrt{n^2 + nm + m^2}/N_R$. The nanotube unit cell is thus formed by a cylindrical surface with height t and diameter d_t. The number of carbon atoms per unit cell can also be expressed as a function of n and m: $N_C = 4(n^2 + nm + m^2)/N_R$.

Once the (n, m) nanotube structure is defined (diameter, chirality, unit cell...), the corresponding graphene strip can be constructed and rolled up into a cylinder. The next step consists in predicting the electronic properties of this (n, m) tube based on the single-band tight-binding model of graphene proposed here. The main advantage of the nearest-neighbor approximation is the very simple analytical expression for the π electronic states of graphene expressed in equation (9), allowing the prediction of the electronic properties of carbon nanotubes using a zone folding approach which does *not* take the curvature of the system into account [58,59].

Due to periodic boundary conditions along the circumferential direction of the tube, the allowed wavevectors "around" the nanotube circumference are quantized: they can only have a set of discrete values. In contrast, the wavevectors along the nanotube axis remain continuous for infinite tubes, presenting an analogous situation as described in the previous section for the ribbons. Plotting these allowed vectors for a given nanotube onto the Brillouin zone of graphene generates a series of parallel lines. The length, the number, and the orientation of these cutting lines depend on the chiral indices (n, m) of the nanotube (Fig. 13). The basic idea behind the zone-folding approximation is that the electronic band structure of a specific nanotube is given by the superposition of the graphene electronic energy bands along the corresponding allowed **k**-lines.

A specific carbon nanotube defines a unique chiral vector $\mathbf{C}_h = (n, m)$ expressed in the basis $(\mathbf{a}_1, \mathbf{a}_2)$ that fixes its symmetry and its diameter. The application of periodic boundary conditions around the tube circumference leads to some restrictions on the allowed wavefunctions quantum phase which imply that carbon nanotubes can be metals or semiconductors with an energy gap that depends on the helicity and on the tube diameter $(1/d_t)$. In the zone folding approximation, the general rules for the metallicity of a single-wall carbon nanotube are as follows: a nanotube defined by the (n, m) indices will be metallic (semiconductor) if $n - m = 3\ell$, with ℓ an integer $(n - m = 3\ell \pm 1)$. Consequently, most carbon nanotubes are semiconductors and only a fraction $(1/3)$ are metallic.

The condition $n - m = 3\ell$ is always satisfied for (n, n) armchair tubes and for the subset of the $(n, 0)$ zigzag tubes with n multiple of 3. Close to E_F, the dispersion relation reads $E^{\pm}(\delta k) \simeq \pm \frac{\sqrt{3}a}{2}\gamma_0 |\delta k|$, presenting a linear energy-momentum relation (Fig. 14) that will be shown to have useful consequences in the transport properties of these nanotubes [60].

The second possible choice for (n, m) nanotubes is given by the condition $n - m = 3\ell \pm 1$ which leads to an obvious gap opening (Fig. 14) at the Fermi level whose value is estimated by

$$\Delta E_g^1 = \frac{2\pi a \gamma_0}{\sqrt{3}|\mathbf{C}_h|} = \frac{2a_{cc}\gamma_0}{d_t}. \quad (16)$$
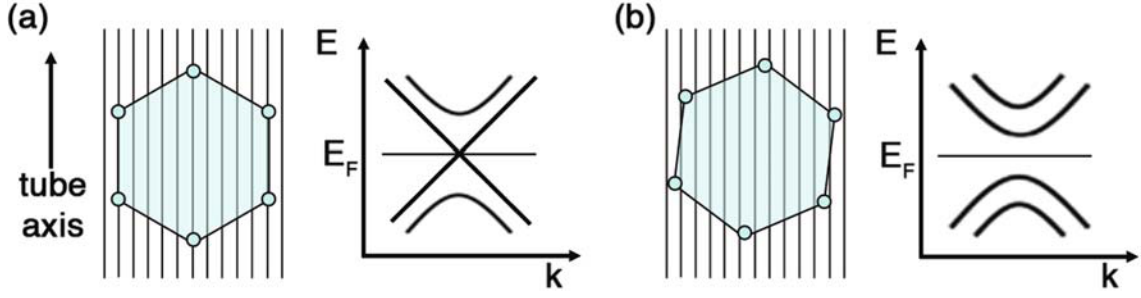
Fig. 14. (Left) metallic nanotube: the allowed **k**-vectors include the K point of the graphene Brillouin zone. The corresponding dispersion relations are linear and exhibit a metallic behavior. (Right) semiconducting nanotube: the K point is not an allowed vector. The corresponding dispersion relation displays an energy gap, illustrating the semiconducting behavior.

It appears that ΔE_g^1 decreases with the inverse of the tube diameter d_t ($d_t = |\mathbf{C}_h|/\pi$). For a very large diameter, one finds as expected a zero gap semiconductor since we recover the graphene sheet. For a realistic $(17, 0)$ tubes with a diameter of 1.4 nm, one gets $\Delta E_g^1 \simeq 0.59$ eV. This $1/d_t$ dependence of the gap on the diameter relies on the assumption of a linear dispersion of the bands around E_F [61]. In reality, the bands are not linear away from E_F, an effect called trigonal warping [62] which induces a dependence of the band gap not only on the diameter, but on the (n, m) indices as well.

In summary, when forming a tube, owing to the periodic boundary conditions imposed in the circumferential direction, only a certain set of **k** vectors in the graphene BZ are allowed. This allowed set of Bloch momentum depends on the diameter and helicity of the tube. Whenever the allowed **k** vectors include the point K, the system is a metal with a nonzero density of states at the Fermi level, resulting in a one-dimensional metal with two bands dispersing linearly close to E_F. When the K point is not included, the system is a semiconductor with a small band gap that depends mainly on the diameter. In this case, the conduction and valence band edges come from states with **k**-vectors located on the allowed line(s) closest to the K point.

As the nanotubes are one-dimensional, their Brillouin zone is one-dimensional as well, with zone edges usually labeled X. Within this band folding approach, the nanotube band structure is thus the $\pi-\pi^*$ bands of graphene within the orthogonal tight-binding scheme along the allowed **k**-lines folded onto the ΓX direction ($\Gamma X'$ with $X' = -X$ is symmetric by time-reversal).

The electronic band structure of an armchair $(5, 5)$ carbon nanotube is presented in Figure 15a. Six bands for the conduction states, and an equal number for the valence one, are observable. However, four of them are degenerate, leading to 10 electronic levels in each case, consistent with the 10 hexagons around the circumference of the $(5, 5)$ nanotube. For all armchair nanotubes, the energy bands exhibit a large degeneracy at the zone boundary, where $k = \pm\pi/a$ (X point), so that equation (9) becomes $E(k = \pm\pi/a) = \pm\gamma_0$. This comes from the absence of dispersion along the segments connecting the neighboring centers of the BZ sides (the M points), an effect that will

yield the so-called trigonal warping of the bands as already discussed. The valence and conduction bands for armchair nanotubes cross at $k = k_F = \pm2\pi/(3a)$, a point that is located at two thirds of ΓX (Fig. 15a). This means that the original **K**-vertices of the original graphene hexagonal BZ are folded at two thirds of the ΓX line (or its inversion symmetry image). As discussed above, the $(5, 5)$ armchair nanotube is thus a zero-gap semiconductor which will exhibit metallic conduction at finite temperatures, since only infinitesimal excitations are needed to promote carriers into the conduction bands.

The density of states (DOS) $\Delta N/\Delta E$ represents the number of available states ΔN for a given energy interval ΔE ($\Delta E \to 0$). This DOS is a quantity that can be measured experimentally under some approximations. The shape of the density of states is known to depend dramatically on dimensionality. In 1D, as shown below, the density of states diverges as the inverse of the square root of the energy ($1/\sqrt{E}$) close to band extrema. These "spikes" in the DOS are called van Hove singularities (VHs) and manifest the confinement properties in the directions perpendicular to the tube axis. As carbon nanotubes are one-dimensional, their corresponding DOS exhibit such a spiky behavior at energies close to band edges (see Fig. 15). For all metallic nanotubes, the density of states per unit length along the nanotube axis is a constant at the Fermi energy (E_F), and can be expressed analytically [63]:

$$\rho(\varepsilon_F) = 2\sqrt{3}a_{cc}/(\pi\gamma_0|\mathbf{C}_h|). \tag{17}$$

The calculated 1D dispersion relations $E(k)$ for the $(9, 0)$ and the $(10, 0)$ zigzag nanotubes are illustrated in Figures 15b, 15c, respectively. As expected, the $(9, 0)$ tube is metallic, with the Fermi surface located at Γ, whereas the $(10, 0)$ nanotube exhibits a finite energy gap at Γ. In particular, in the case of the $(10, 0)$ nanotube, there is a dispersionless energy band at $E/\gamma_0 = \pm1$, which gives a singularity in the DOS at these peculiar energies. For a general $(n, 0)$ zigzag nanotube, when n is a multiple of 3, the energy gap at $k = 0$ (Γ-point) becomes zero. However, when n is *not* a multiple of 3, an energy gap opens at Γ. The corresponding densities of states have a zero value at the Fermi energy for the semiconducting nanotube, and a small non-zero value for the metallic one.

Note that the k values for the band crossing at E_F in metallic nanotubes are $k = \pm2\pi/3T$ or $k = 0$ for armchair
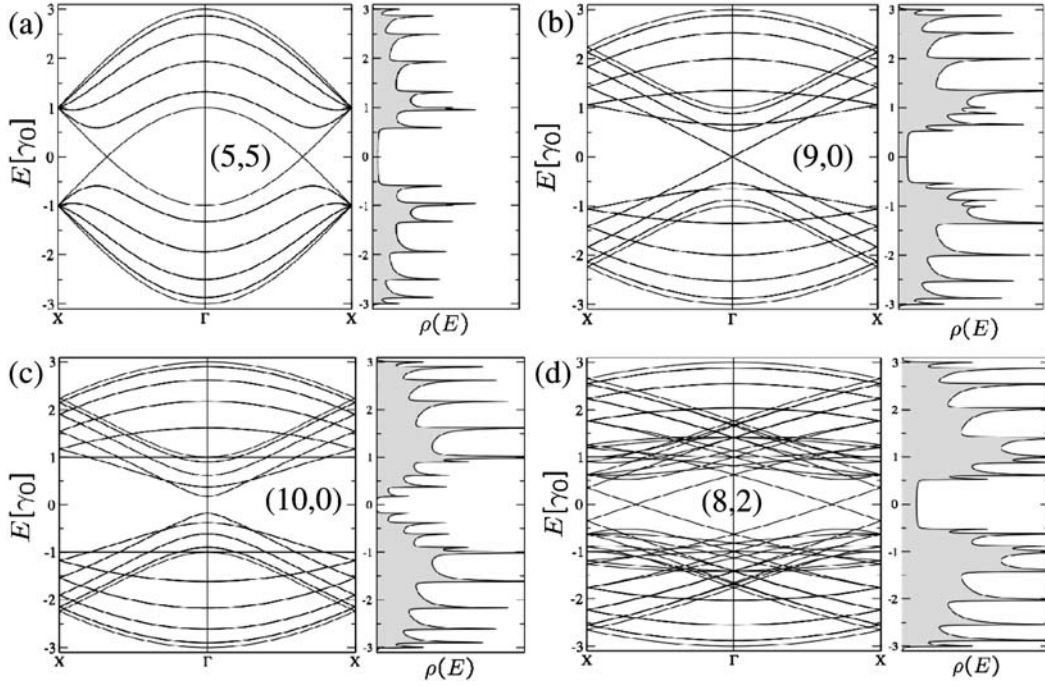
Fig. 15. Band structure and density of states for (a) a $(5,5)$ armchair nanotube (b) a $(9,0)$ zigzag nanotube, (c) a $(10,0)$ zigzag nanotube, and (d) a $(8,2)$ chiral nanotube within the zone folding model. The 1D energy dispersion relations are presented in the $[-3\gamma_0; 3\gamma_0]$ energy interval in dimensionless units (γ_0 being the nearest neighbor C–C tight-binding overlap energy $\sim$2.9 eV). The energy bands are plotted along the $X-\Gamma-X$ direction. The Fermi level is located at zero energy. Adapted from reference [13].

or zigzag tubes, respectively. These k-values are also the locations of the band gaps for the semiconducting zigzag nanotubes. The same k-values denote as well the positions of the energy gaps (including zero energy gaps) for the general case of chiral nanotubes. In Figure 15d, the dispersion relations $E(k)$ for the $(8,2)$ chiral nanotube are illustrated. Since $n-m$ is a multiple of 3, this nanotube exhibits a metallic behavior with a band crossing at $k = \pm 2\pi/3T$. Other chiral nanotubes, like the $(9,6)$ (not shown), display a zero energy gap at $k = 0$. The DOS of chiral nanotubes (see Fig. 15d) also displays van Hove singularities as for the achiral tubes [64].

In semiconducting zigzag or chiral nanotubes, the band gap (as expressed in Eq. (16)) is independent of the chiral angle and varies inversely with the nanotube diameter: $\Delta E_g^1 = 2\gamma_0 a_{cc}/d_t$ (in the linear bands approximation). Density of states measurements by scanning tunneling spectroscopy (STS) provide a powerful tool for probing the electronic structure of carbon nanotubes. It can be shown indeed that under some assumptions, the voltage-current derivative dI/dV is proportional to the DOS. These experiments [65,66] confirmed that the energy band gap of semiconducting tubes is roughly proportional to $1/d_t$, and that about $1/3$ of nanotubes are conducting, while the other $2/3$ are semiconducting. Resonances in the DOS have also been observed experimentally [65,66] on both metallic and semiconducting nanotubes whose diameters and chiral angles were determined using a scanning tunneling microscope (STM) [67]. Several other experimental techniques such as resonant Raman scattering [68], opti-

cal absorption and emission measurements [69–71], have also confirmed this structure in van Hove singularities of the electronic densities of states in singlewall nanotubes.

Curvature effects: beyond the zone folding model

The preceding section proposes a model for the electronic properties of SWNTs, based on the confinement of the electrons around the tube circumference, allowing a selection on the allowed **k** Bloch vectors. As a matter of fact, since the states selected in the band folding scheme were the ones of the planar graphene sheet, curvature effects are just neglected. However, carbon nanotubes are not just stripes of graphene but small cylinders. The carbon atoms are placed onto a cylindrical wall, a topology which induces several effects as compared to the planar graphene sheet: (I) the C–C bonds perpendicular and parallel to the axis are slightly different, so that the $\mathbf{a}_1$ and $\mathbf{a}_2$ basis vectors have now different length, (II) these bond length changes, and the formation of an angle for the two p_z orbitals located on bonds not strictly parallel to the axis, yield differences in the three hopping terms γ_0 between a carbon atom with its three neighbors and (III) the planar symmetry is broken so that the π and σ states can mix and form hybrid orbitals that exhibit partial sp^2 and sp^3 character. Such a curvature effect is *not* taken into account in the zone folding model of graphene where the π orbitals cannot mix with the σ states as they show
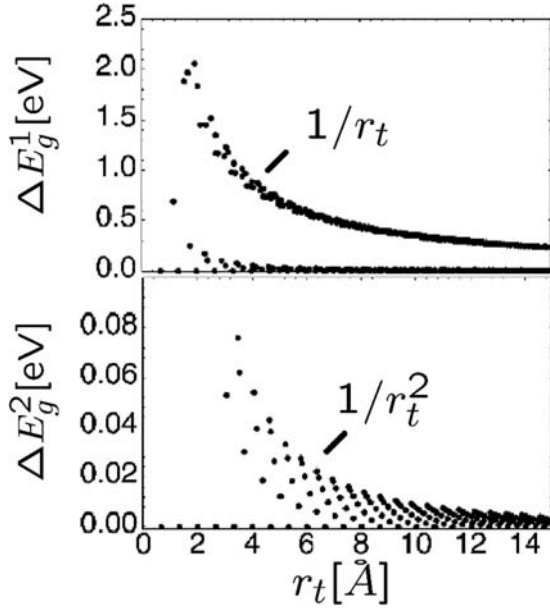
Fig. 16. Magnitude of both primary (E_g^1) and secondary (E_g^2) gaps in carbon nanotubes with radii less than 15 Å. The primary gap (ΔE_g^1) scales as $1/R$ (top panel). The secondary gap (ΔE_g^2 or curvature induced gap) scales as $1/R^2$. The dots at $\Delta E_g^1 = \Delta E_g^2 = 0$ correspond to the armchair nanotubes which always preserve their metallic character. Adapted from reference [72].

different parity with respect to planar reflexion. In the present section, the effect of the finite curvature on the electronic properties of singlewall nanotubes is investigated.

The effects labeled (I) and (II) modify the conditions which define the **k**-point at which occupied an unoccupied bands do cross (a point labelled k_F), and shift this Fermi vector k_F away from the Brillouin zone corners (K-point) of the graphene sheet [72]. For armchair nanotubes, taking curvature into account shifts the Fermi wave vector along an allowed line of the graphene Brillouin zone. Consequently, for symmetry reasons, armchair tubes always preserve their metallic character with finite curvature. However, for "metallic" non-armchair nanotubes, k_F moves away from the K-point perpendicularly to the allowed **k**-lines such that the allowed 1D subband no longer passes through k_F, opening a very small band gap at E_F (see Fig. 16).

In summary, when accounting for curvature effects, the only zero-band gap tubes are the (n,n) armchair nanotubes. (n,m) tubes with $n-m = 3\ell$, where ℓ is a nonzero integer, are "tiny-gap" semiconductors. Armchair tubes are sometimes labeled "type I" metallic tubes, while the others are of "type II". All other nanotubes are intermediate gap (a few tenths of an eV) semiconductors. For the tiny-gap semiconducting nanotubes, the so-called secondary gap (due to the curvature) obviously depends on the diameter and the chiral angle, and scales as $1/d_t^2$ [72]. For the quasi-metallic zigzag nanotubes (chiral angle $= 0$),

this secondary gap is given by:

$$\Delta E_g^2 = \frac{3\gamma_0 a_{cc}^2}{4d_t^2} \qquad (18)$$

and is so small that, for most practical purposes, all the $n - m = 3\ell$ tubes can be considered as metallic at room temperature (see Fig. 16). Density of states measurements by scanning tunneling spectroscopy [73] confirm the expected $1/d_t^2$ dependence for three zigzag nanotubes, and that armchair nanotubes remain truly metallic. Consequently, the band-folding picture, based on the single-band tight-binding approach [58–60], continues to be valid for large diameter tubes.

For very small tubes, the curvature is so strong that some rehybridization among the σ and π states appears (effect III mentioned above). In such a case, the zone-folding picture may fail completely and either an extended *tight-binding* approach [74,75] or ab initio calculations [76] should be performed to predict the electronic properties of small diameter nanotubes. First-principles pseudopotential local density functional (LDA) calculations indeed revealed that sufficiently strong hybridization effects can occur in small radius nanotubes which significantly alter their electronic structure. Strongly modified low-lying conduction band states are introduced into the band gap of insulating tubes because of hybridization of the σ^* and π^* states. As a result, the energy gaps of some small radius tubes are decreased by more than 50%. In the specific case of the $(6,0)$ tube, which is predicted to be a semimetal in the band-folding scheme, a singly degenerate hybrid $\sigma^*-\pi^*$ state is found to lie 0.83 eV (at Γ) below the doubly degenerate state that forms the top of the valence band in the zone-folding model. This band overlap makes the $(6,0)$ tube a true metal within LDA, with a density of states at the Fermi level equal to 0.07 state/eV atom. The $\sigma^*-\pi^*$ hybridization can be clearly observed by drawing the charge density associated with the states around the Fermi level. Such states are no longer antisymmetric with respect to the tube wall, with a clear "charge spilling" out of the tube. For nanotubes with diameters greater than 1 nm, these rehybridization $\sigma-\pi$ effects are unimportant. Further, as discussed above, symmetry considerations suggest that armchair tubes are less affected by such rehybridization.

At last, ultrasmall radius single-wall carbon nanotubes (diameter of about 4 Å) have been synthesized by confining their synthesis inside inert AlPO$_4$-5 zeolite channels (with inner diameter of about 7.3 Å) [77]. The diameter of these tubes gives them many unusual properties such as superconductivity [78]. Such a narrow diameter distribution around 4 Å, reduces the potential carbon nanotube (CNT) candidates to three: the $(3,3)$, $(4,2)$, and $(5,0)$. The properties of these ultrasmall tubes have been extensively investigated by ab initio simulations [79]. In particular, it was shown that the $(5,0)$ tube, expected to be semiconducting following the band folding picture, is actually a metal with two bands (one doubly degenerate) crossing the Fermi level (yielding two different k_F). This is a clear manifestation of curvature effects due to a Peierls

distortion. The armchair $(3,3)$ tube remains semimetallic, but with a $\pi-\pi^*$ band crossing at E_F that is displaced off its ideal $2\Gamma X/3$ position, confirming as described above that armchair tubes are much less sensitive to curvature effects.

In conclusion, the zone-folding model remains valid when the diameter of the nanotube is greater than 1 nm. When this condition is not satisfied, the single-band tight-binding approach may fail completely and more accurate calculations based on an extended *tight-binding* approach or ab initio should be performed to predict the electronic properties of these small diameter nanotubes.

5 Quantum transport in 1D carbon nanostructures

5.1 Quantum transport in carbon nanotubes

Coherent quantum transport in mesoscopic and low-dimensional systems can be rigorously investigated either with the Kubo-Greenwood [80] or the Landauer-Büttiker formalisms [81]. The first approach, that derives from the fluctuation-dissipation theorem, allows to evaluate the intrinsic conduction regimes within the linear response, and gives a direct access to the fundamental transport length scales, such as the elastic mean free path (ℓ_e) and the localization length (ξ). While ℓ_e results from the elastic backscattering driven by static perturbations (defects, impurities) of an otherwise clean crystalline structure, ξ denotes the scale beyond which quantum conductance decays exponentially with the system length (L), owing to the accumulation of quantum interference effects that progressively drive the electronic system from weak to strong localization. The coherence length L_ϕ gives the scale beyond which localization effects are fully suppressed owing to decoherence mechanisms, such as electron-phonon (e–ph) or electron-electron (e–e) couplings, treated as perturbations on the otherwise noninteracting electronic gas (weak localization regime). When ℓ_e becomes longer than the length of the nanotube in between voltage probes, the carriers propagate ballistically, and contact effects prevail. In such a situation, the Landauer-Büttiker formalism becomes more appropriate, since it rigorously treats transmission properties for open systems and arbitrary interface geometries. Besides, its formal extensions (Non Equilibrium Green's Functions-NEGF and Keldysh formalism) further enable to investigate quantum transport in situations far from the equilibrium, of relevance for high-bias regimes or situations with dominating contribution of Coulomb interactions [82]. Interestingly, to investigate coherent quantum transport in a ribbon or a nanotube of length L with reflection-less contacts (ideal contact) to external reservoirs, both transport formalisms are formally fully equivalent.

In the following, the Landauer-Büttiker formalism will be used and the corresponding conductance will be evaluated from the transmission coefficient:

$$T(E) = \text{tr}\{\hat{\Gamma}_L(E)\hat{G}^{(+)}_{\text{tube}}(E)\hat{\Gamma}_R(E)\hat{G}^{(-)}_{\text{tube}}(E)\} \quad (19)$$
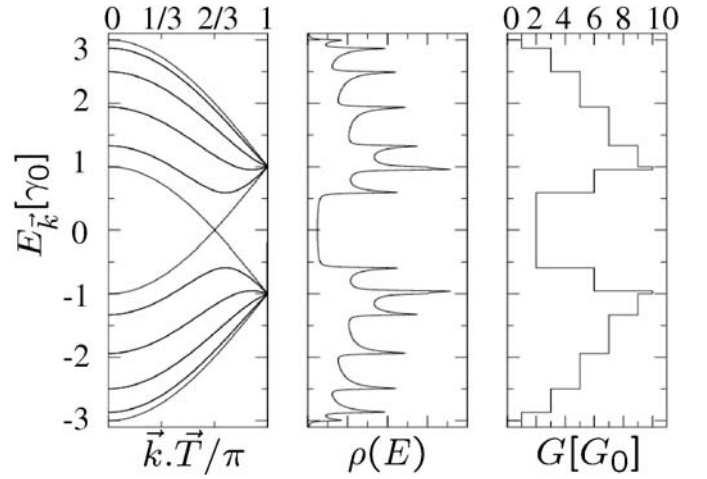

Fig. 17. Band structure (left), density of states (middle) and conductance (right) for the $(5,5)$ armchair nanotube based on the single-band folding model. Adapted from reference [13].

given as a function of the retarded Green function $\hat{G}^{(+)}(E) = \{E\hat{I} - \hat{H} - \hat{\Sigma}_L(E) - \hat{\Sigma}_R(E)\}^{-1}$ and $\hat{\Sigma}_R(\hat{\Sigma}_L)$ the self energy accounting for the coupling with the right (left) electrode [82]. The Landauer-Büttiker formula can be indifferently implemented with effective models, such as a tight-binding Hamiltonian, or a Hamiltonian derived from first-principles. Indeed, the ab initio electronic transport calculations presented in the following are performed within the non-equilibrium Green's functions formalism and using the one-particle Hamiltonian obtained from the DFT calculations as implemented in the SMEAGOL code [83]. When defects are concerned, the defective supercells are connected to perfect nanotube- or ribbon-based leads. In order to simulate open boundary conditions, the self-energies associated with the leads are then included within the self-consistent calculation of the potential. Finally, the electronic transmission functions are evaluated by using of the Fisher-Lee relation [84]. Note that, for the computation of the transmission functions, a $25 \times 1 \times 1$ supercell is considered in order to obtain a good screening of the perturbed Hartree potential due to the defect. Experimentally, it is possible to investigate the energy dependence of the conductance by modulating the density of charge using a capacitive coupling between the nanostructure channel and an external gate.

For a carbon nanotube of length L in between metallic contact reservoirs, the transport regime is ballistic if the measured conductance is L-independent, and only given by the energy-dependent number of available quantum channels $N(E)$ times the conductance quantum $G_0 = 2e^2/h$, that is $G(E) = 2e^2/h \times N(E)$, including spin degeneracy. This occurs only in case of perfect (reflection-less) or ohmic contacts between the CNT and metallic voltage probes. In this regime, the expected energy-dependent conductance spectrum is easily deduced, from band structure calculations, by counting the number of channels at a given energy. For instance, metallic armchair nanotubes present two quantum channels at the Fermi
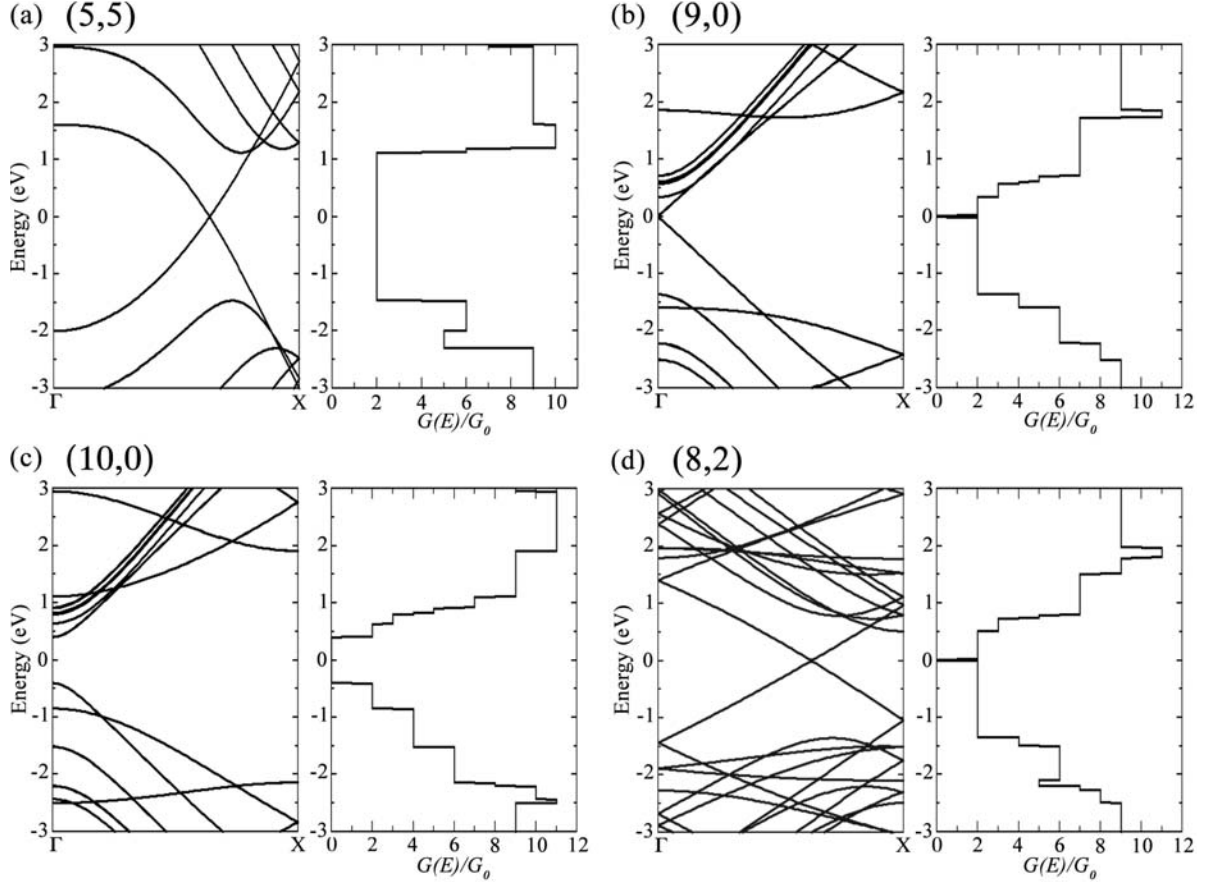
Fig. 18. Band structures and quantum conductances of (a) $(5,5)$ armchair, (b) $(9,0)$ and (c) $(10,0)$ zigzag, and (d) $(8,2)$ chiral nanotubes, based on first-principles calculations.

energy $E_F = 0$, or charge neutrality point, resulting in $G(E_F) = 2G_0$. At higher energies, the conductance increases as more channels become available to conduction. For illustration, the electronic bands and conductance of the $(5,5)$ metallic tube are displayed in Figure 17 within the symmetric $\pi-\pi^*$ tight-binding model.

This quantum conductance of armchair carbon nanotubes within a nearest-neighbor π-orbital tight-binding Hamiltonian is in good agreement with ab initio calculations as illustrated in Figures 18a. Indeed the $(5,5)$ armchair carbon nanotube is found to be a metallic nanowire with two linear electronic energy bands which cross at the Fermi level and contribute two conductance quanta ($=4e^2/h$) to the conductance when the tube is defectless. These two quantum channels at the charge neutrality point also lead to a plateau of conductance on a quite important interval of energies ($\sim$2.5 eV).

In Figures 18b and 18c, the ab initio electronic properties and the corresponding electronic conductance are presented for a $(9,0)$ and $(10,0)$ zigzag nanotubes, respectively. Again, the first-principles calculations confirm the general features of the electronic structure obtained in the tight-binding approach. Indeed, as mentioned previously, the opening of a secondary gap (pseudogap) at the Fermi energy produced by the curvature of the graphitic walls in the $(9,0)$ nanotube can be observed. In the $(10,0)$ case, is

predicted to exhibit a semiconducting behavior, a primary gap of 0.8 eV is predicted, leading to a zero transmission for that specific energy window. At last, in order to be as exhaustive as possible, the ab initio electronic properties and the conductance of the $(8,2)$ are illustrated in Figures 18d. Although the single-band model would have proposed a metallic tube, the first-principles calculations predict a semiconducting system with a very small pseudogap related to the curvature of the nanotube, as for the $(9,0)$ nanotube.

However, all these ab initio values predicted for the conductance are the uppermost theoretical limits that would be experimentally measured. In practical situations, lower values are observed since reflection-less transmission at the interface between the voltage probes (metallic leads) and the nanotubes is fundamentally limited by interface symmetry mismatch, inducing Bragg-type backscattering. Additionally, topological and chemical disorders, as well as intershell coupling, introduce intrinsic backscattering along the tube, which also reduce its transmission capability. To account for both effects, one generally introduces $T_n(E) \leq 1$, the transmission amplitude for a given channel, at energy E, so that $G(E) = G_0 \sum_{n=1,N_\perp} T_n(E)$ [82], as illustrated in the following for the case of topological defects and doping in carbon nanotubes.
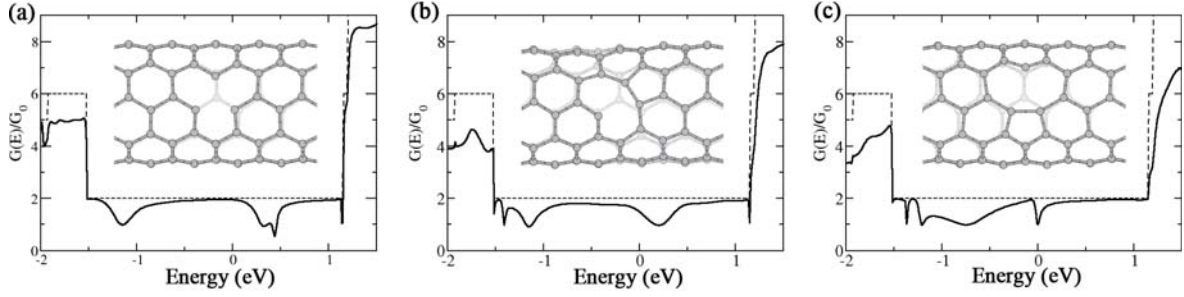
Fig. 19. Quantum ab initio conductance of a $(5,5)$ armchair nanotube containing (a) a bare D_{3h} monovacancy and a reconstructed C_s vacancy in two different positions: (b) tilted or (c) perpendicular to the axis of the tube. Atomic structures of the corresponding defects are shown in insets.

The effects of impurities and local structural defects on the conductance of metallic carbon nanotubes have been calculated using ab initio techniques within the Landauer formalism [85]. For example, with a point (single-atom) vacancy, the conductance shows one broad dip (valence region) and two narrower dips (conduction region) as illustrated in Figure 19a. The reduction of conductance at the broad dip is $1G_0$ with approximately half reflection of both π and π^* bands. Because a single impurity breaks the mirror symmetry planes containing the tube axis, an eigenchannel is a mixture of the π and π^* bands. Consequently, an electron in an eigenchannel here is either completely reflected or completely transmitted. The location of the broad dip in the present ab initio calculation (-1.2 eV with respect to the charge neutrality point) is quite different from the results obtained by the single-band tight-binding model which predicts a single dip exactly at the Fermi level [86]. However, electron-hole symmetry is no longer valid in a more realistic ab initio calculation, and the dip position moves. Moreover, two other narrower dips are observed closer to E_F and originate from resonant scattering by quasibound states derived from the broken σ bonds around the vacancy (Fig. 19a). The σ bonds between the removed atom and its neighbors are broken, and dangling bonds are produced which are mainly composed of π orbitals parallel to the tube surface. Since σ-bond states are orthogonal to the π valence band states, a very weak coupling is present between them. Among three quasibound states derived from three dangling bonds, one is an s-like bonding state which lies well below the first lower subband (outside the scope of the figure). The other two states are orthogonal to it (i.e., partially antibonding) and give rise to the two narrower dips in the conduction region as shown in Figure 19a. However, the interaction among the dangling σ bonds causes substantial atomic relaxations, thus inducing the reconstruction of the bare monovacancy (D_{3h} symmetry) into a more stable vacancy structure exhibiting C_s symmetry (Figs. 19b, 19c) [87]. More specifically, the D_{3h} vacancy undergoes a Jahn-Teller distortion upon relaxation, where two of the atoms near the vacancy move closer, forming a pentagon-like structure while the third atom is slightly displaced out of the plane. In addition, the vacancy can adopt two different positions related to the hexagonal network of the nanotube: a tilted position (Fig. 19b) or a perpendicular position (Fig. 19c)
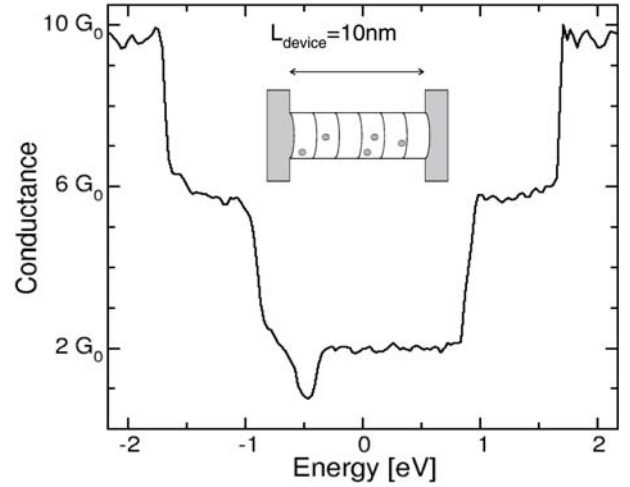
Fig. 20. Effects of a 0.1% concentration of boron substitutional impurity on the conductance of a $(10,10)$ carbon nanotube. The conductance as a function of the incident energy E displays a large dip located in the $2G_0$ plateau of the tube, located in the valence band region (-0.5 eV with respect to E_F). A hundred carbon atoms are randomly substituted by boron dopants in a 2500 cells nanotubes (100 000 sites). This 10 nm doped nanostructure is schematically illustrated in the inset. Adapted from reference [89].

regarding the axis of the nanotube. The tilted vacancy is found to be the most stable configuration with a $\Delta E = 1.34$ eV energy difference compared to the perpendicular case [88]. However, both vacancies have a significant influence on the electronic structure of the tube, imposing important backscattering to incoming electrons at specific energies. In fact, the accurate positions of the vacancy-related quasibound state levels depend on various factors such as its atomic configuration, its orientation versus the axis of the tube, and the nanotube diameter [85].

Identically, substitutionally doped boron or nitrogen produces quasibound impurity states of a definite parity and reduces the conductance by a quantum unit $2e^2/h$ via resonant backscattering [85]. The conductance of a $(10,10)$ carbon nanotube with a 1% concentration of boron impurity is calculated using tight-binding methods correlated to ab initio calculations [89] and is presented in Figure 20. The conductance of the doped tube is found to be virtually
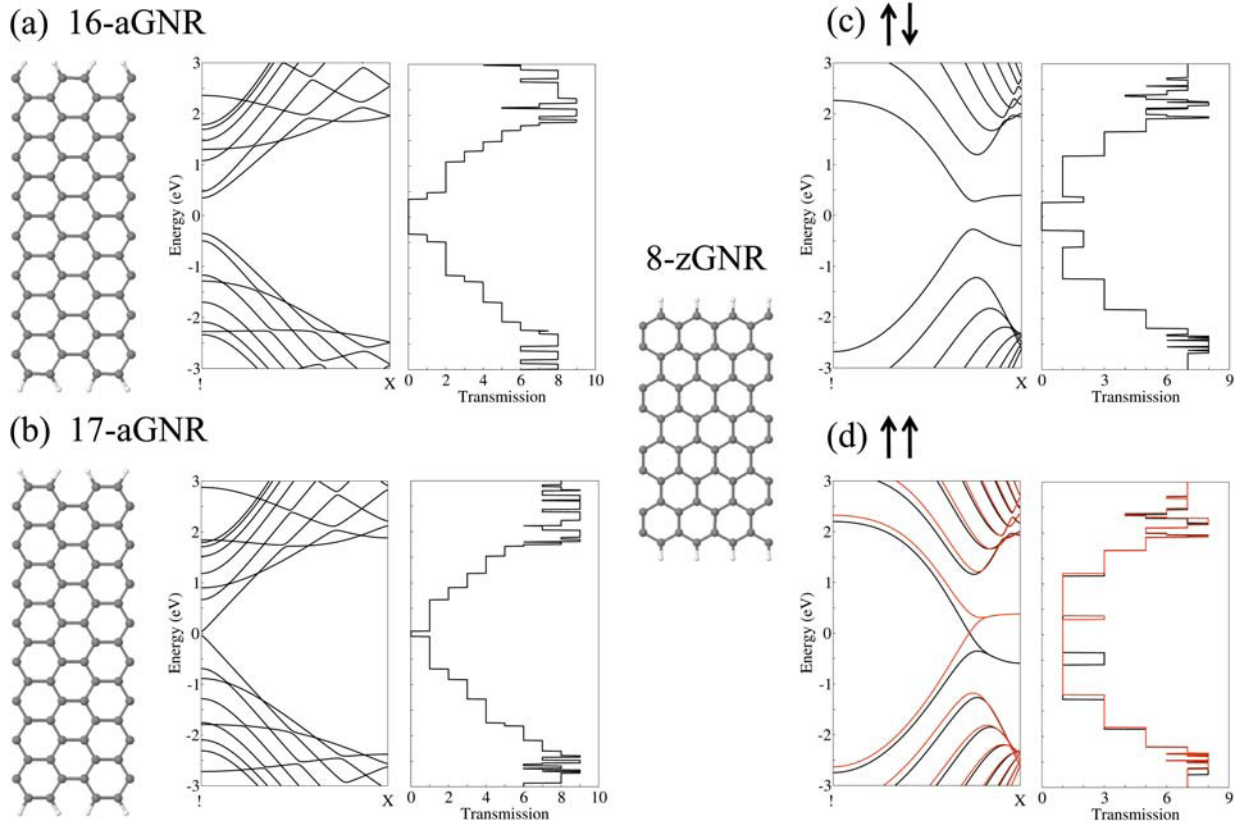
Fig. 21. Atomic structures, electronic band structures and quantum conductances (electronic transmission) of various graphene nanoribbons: (a) 16-armchair GNR, (b) 17-armchair GNR, 8-zigzag GNR with (c) anti-parallel (↑↓) or (d) parallel (↑↑) spin orientations between the two magnetic edges. The spin-dependent transport is evaluated for both magnetic configurations of the 8-zGNR (c–d) but is only visible for the parallel (↑↑) spin orientations (ferromagnetic one). In such case, one spin orientation is labeled α-spin (in black) while the other is labeled β-spin (in red).

unchanged at E_F, meaning that the impurity potential does not scatter incoming electrons at this energy. On the other hand, a quite pronounced dip is observed in the conductance below. The amount of reduction at this dip is $1G_0$. A nitrogen substitutional impurity has similar effects on conductance, but on the opposite site of the charge neutrality point [85]. These resonant states of dopants in nanotube suggest strong similarities to acceptor or donor states in semiconductors.

Generic transport properties such as conduction mechanisms, mean-free paths, and conductance scalings can be derived using a Kubo-Greenwood real-space approach [89] for various concentration of randomly distributed boron and nitrogen dopants. For a low density of dopants yields diffusive regimes, with a mean-free path decreasing linearly with dopant concentration following the Fermi golden rule, and increasing linearly with nanotube diameter. Moreover, the estimated electronic mean-free paths are in the order of 175–275 nm for boron-doped nanotubes with diameters in the range 23 nm and 1.0% of doping, in good agreement with experimental data. Consequently, a small amount of dopants (≪0,5%) can drastically modify the electronic transport properties of the nanotube, which is certainly a key effect feature for envisioning nanoelectronics.

5.2 Quantum transport in carbon nanoribbons

In contrast to carbon nanotubes, quantum transport properties of GNRs are expected to strongly depend on whether their edges exhibit the armchair or the zigzag configurations. Indeed, in the previous sections, the electronic properties of GNRs have been predicted using the single-band model and ab initio calculations, revealing a dependence on the edge topology [28]. The armchair GNRs are semiconductors with energy gaps which decrease as a function of increasing ribbon widths. As mentioned earlier, the gaps of the N-aGNRs depend on the N value, separating the ribbons in three different categories (all exhibiting direct band gaps at Γ). The band structures and the corresponding quantum conductances of two armchair GNRs are illustrated in Figures 21a, 21b. The 16-aGNR is a ∼0.8 eV gap semiconductor, thus inducing a quite large energy interval where no transmission is allowed (Fig. 21a), while the gap of the 17-aGNR is reduced to less than 0.2 eV (Fig. 21a). The region of zero conductance is also reduced accordingly, and a very small external electric field would induce an electronic transmission through one channel ($1G_0$ for the conductance). Identically, nanoribbons with zigzag shaped edges also exhibit direct band gaps which decrease with increasing width. However, in zGNRs, quantum transport is dominated by

(a)   zGNR ↑↓ + adatom

(b)   zGNR ↑↓ + vacancy

(c)   zGNR ↑↑ + adatom

(d)   zGNR ↑↑ + vacancy
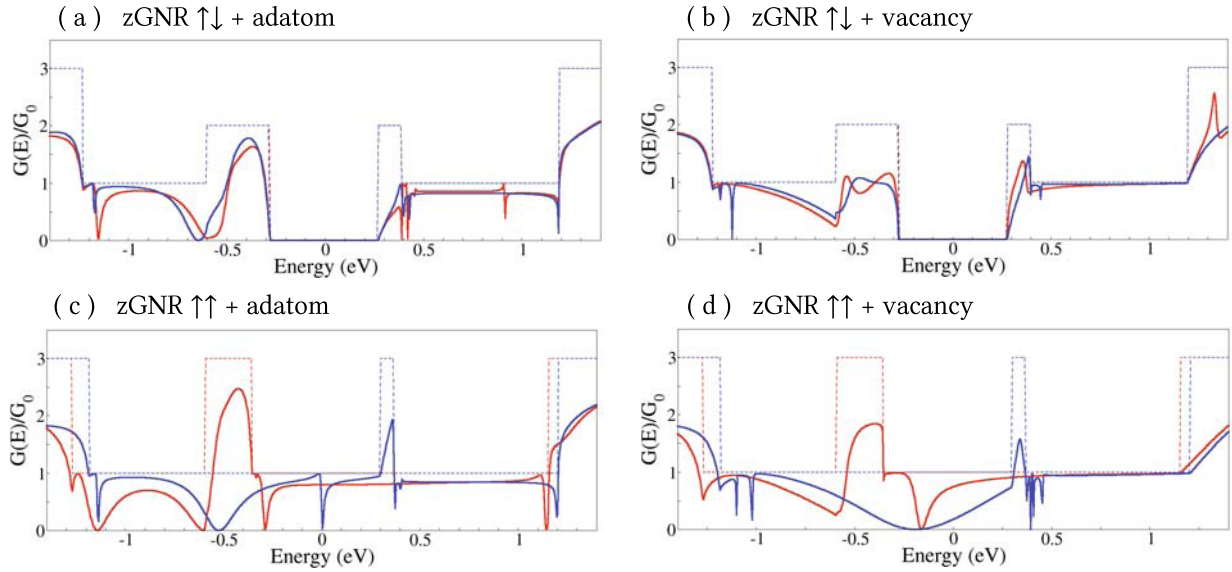
Fig. 22. Electronic transmission functions of a 8-zGNR in the presence of an isolated carbon adatom (a)–(c) or an isolated vacancy (b)–(d) localized around the ribbon axis, in either the a ↑↓ configuration (a)–(b) or the ↑↑ configuration (c)–(d) of the ribbon edges. The spin α and spin β components are presented in blue and red, while the dotted line indicates the number of π channels in the pristine nanoribbon.

edge states which are expected to be spin-polarized owing to their high degeneracy. Indeed, due to topological reasons, zigzag-shaped edges give rise to peculiar extended electronic states which decay exponentially inside the graphene sheet [28]. These edge-states, which are not reported along the armchair-shaped edges, come with a twofold degenerated flat band at the Fermi energy over one third of the Brillouin zone. The ground state of zGNRs with hydrogen passivated zigzag edges presents finite magnetic moments on each edge with negligible change in atomic structure [38], thus suggesting zGNRs to be attractive for spintronics [39]. Indeed, upon inclusion of the spin degrees of freedom within ab initio calculations (LSDA), the zGNR are predicted to exhibit a magnetic insulating ground state with ferromagnetic ordering at each zigzag edge and antiparallel spin orientation between the two edges [38]. The total energy difference between ferromagnetic (↑↑) and antiferromagnetic (↑↓) couplings between the edges is of the order of ∼10 meV per edge atom for a 8-zGNR, however, decreases as the width of the ribbon increases and eventually becomes negligible if this width is significantly larger than the decay length of the spin-polarized edge states [33]. Because the interaction between spins on opposite edges increases with decreasing width, the total energy of an N-zGNR with antiferromagnetic arrangement across opposite edges is always lower than that of a ferromagnetic arrangement for low value of N ($N \leq 30$). The band structures and the spin-dependent quantum conductances of a 8-zGNR are illustrated in Figures 21c, 21d in the two respective magnetic configurations (↑↓ and ↑↑) of the ribbon edges. The ↑↓ spin configuration of the 8-zGNR conserve the semiconducting behavior of the GNR family, and its electronic transmission function displays a gap of 0.5 eV around the Fermi energy (Fig. 21c). On the contrary, in the ↑↑ spin config-

uration, the 8-zGNR becomes metallic, inducing a non-zero electronic transmission function at the Fermi energy (Fig. 21d). In addition, the spin-dependent conductance calculation also reveals that the transmission of π electrons with one type of spin orientation (α-spin) is favored for a energy region around −0.5 eV below the charge neutrality point. On the contrary, π^* electrons with the other orientation (β-spin) are more easily transmitted around +0.3 eV above the Fermi energy.

However, ideal zigzag GNRs are not efficient spin injectors due to the symmetry between the edges with opposite magnetization. In order to obtain net spin injection, this symmetry must be broken [90]. Incorporating defects (such as vacancies or adatoms) in the GNR or imperfections at the edge which usually cannot be avoided experimentally, break the symmetry between the edges and could thus influence the spin conductance of the GNR. In addition, the introduction of magnetic point defects in zGNRs favors a specific spin configuration of the edges. As an example, the ↑↑ spin configuration is favored when vacancies or adatom are introduced around the ribbon axis. Consequently, point defects are also expected to play a key role on the transport properties of zGNRs [91]. Ab initio calculations of the electronic transmission functions are performed within the Landauer approach using a supercell containing the point defect connected to two leads consisting of a few unit cells of ideal 8-zGNR. Both the (↑↓) semiconducting and the (↑↑) metallic spin configurations of the ribbon are considered (Fig. 22).

The main impact of the magnetic point defects on the transport properties is a global reduction of the transmission associated with the π and π^* electrons. This is related to a decrease of the transmission probability of some $\pi−\pi^*$ conduction eigenchannels compared to the pristine 8-zGNR. Within the (↑↓) semiconducting configuration
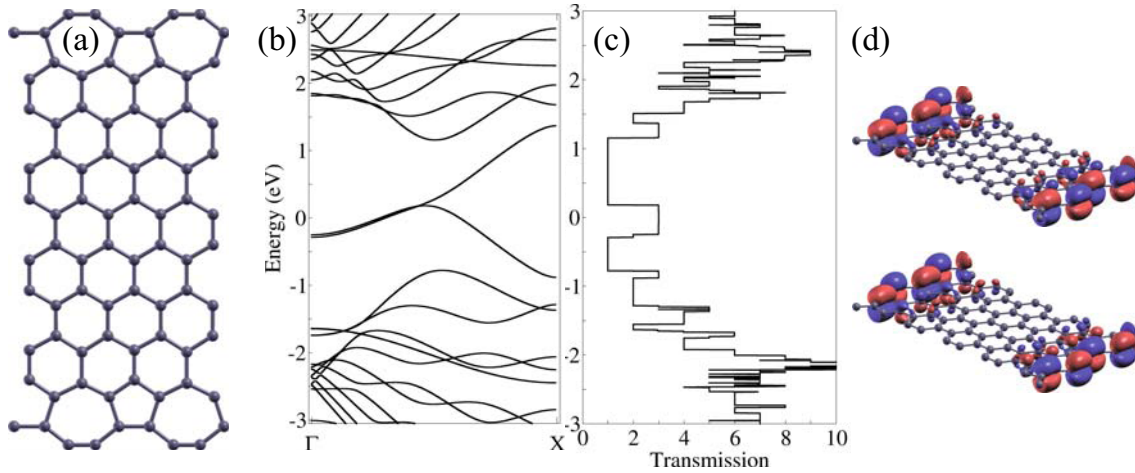
Fig. 23. Atomic structure model (a), electronic band structure (b) and quantum conductance (c) of a 8-zGNR with a reconstructed edge containing pentagons and heptagons (zz57). The π electronic states surrounding the Fermi energy are represented in (d) and are found to be mainly localized on the zz57-reconstructed edge.

(Figs. 22a and b), the presence of defects essentially reduces the conductance for energies ranging from -0.80 to -0.3 eV (π channels) and from 0.3 to 0.5 eV (π^* channels), inducing a slight breaking of the spin degeneracy. Within the ($\uparrow\uparrow$) metallic configuration, a similar reduction of the conductance is observed (Figs. 22c and 22d). However, the defects also induces sharp drops in the transmission function around the Fermi level. At these energies, the electronic states localized on the defect are spin polarized and can only mix with one of the two spin conduction channels. Consequently, the spin-degeneracy of the electronic transmission function is lifted up just around the Fermi energy. In summary, when adatoms and vacancies are introduced, the parallel spin orientation may be preferred and the local magnetic moment of the defect adds up to the contributions of the edges. Furthermore, a spin-polarized transmission is observed at the Fermi energy, suggesting the use defect-doped graphene nanoribbons as spin-valve device (or spin-filter) in future spin-based electronics.

In contrast to carbon nanotubes, GNRs exhibit a high degree of edge chemical reactivity, which, for instance, prevents the existence of truly metallic nanoribbons [50,92,93]. Additionally, the discrepancy between the theoretical electronic confinement gap and the experimentally measured transport gap has been attributed to localized states induced by edge disorder [94,95]. Several experimental studies have also reported the characterization of individual edge defects either by means of Raman, scanning tunneling or transmission electronic microscopy [42,96–98]. To date, several defect topologies of edge disordered (reconstruction and chemistry) have been proposed for GNRs, and ab initio calculations have evidenced the stability of certain types of geometries such as the Stone-Wales reconstruction [44,99,100]. Indeed, at room temperature, the zigzag edge is found to be metastable and a planar reconstruction implying pentagons and heptagons (zz57) spontaneously takes place (Fig. 23a). Such a zz57-reconstruction self-passivates the edge with respect to adsorption of atomic hydrogen from

a molecular atmosphere. Indeed, the formation of triple bonds with alternating single bonds is suggested by the nearly isolated dimers at the ribbon edge, thus removing the dangling bond bands (due to the absence of hydrogen) away from the Fermi level by lifting the degeneracy almost by 5 eV [99]. Because the dangling bond bands shift to elusive energies, the corresponding chemical reactivity is also reduced, stabilizing the zz57 edge. This zz57-reconstruction also modifies the electronic structure of the ribbon. The presence of the edge states around the Fermi level (Fig. 23b) makes this reconstruction ideal for conductance measurements, in contrast to armchair ribbons where the edge state is absent. Indeed, ab initio quantum conductance of a zz57 reconstructed 8-zGNR has been calculated and is presented in Figure 23c. The electronic transmission is predicted to be quite high at the charge neutrality point ($G = 3G_0$), compared to the conventional conductance ($G = 1G_0$) predicted for pristine zGNRs at the Fermi Energy (Fig. 21d). In zz57-edge reconstruction, π electrons are easily transmitted and these electronic channels are localized at the zz57-reconstructed edge (Fig. 21d). Consequently, this novel thermodynamically and chemically stable reconstruction could play a key role in the formation of angular joints in nanoribbons [6]. The knowledge of the atomic structure and the stability of the possible ribbon edges is a crucial issue to control the experimental conditions of the formation of graphene nanoribbons of desired properties for future nano-electronics.

At last, doping may also be used to taylor the electronic and transport properties of GNRs. In carbon-based materials, p-type (n-type) chemical doping can be achieved by boron (nitrogen) atom substitution within the carbon matrix, leading to interesting nanodevice which are crucial for building logic functions and complex circuits [101]. As previously mentioned for metallic carbon nanotubes, boron (B) and nitrogen (N) impurities yield quasibound states that strongly backscatter propagating charge for specific resonance energies [85]. In contrast with

CNTs, doping in GNRs turns out to display more complex features depending on the dopant position, ribbon width, and symmetry. Indeed, the energies of the quasibound states in GNRs are strongly dependent on the position of the impurity with respect to the ribbon edges [102]. Binding energies of the bound state associated with the broad drop in the conductance are found to increase as the dopant approaches the edge of the ribbon. The large variation of resonant energies with dopant position indicates that random distribution of impurities will lead to a rather uniform reduction of conductance over the occupied states part of the first conduction plateau [102]. These predictions are in sharp contrast to the case of CNTs, where resonant energies do not depend on the position of the dopant around the tube circumference. In addition, doping effects are also found to depend on the ribbon symmetry and width, leading for example to a full suppression of backscattering for symmetry preserving impurity potentials in armchair ribbons. Finally, chemical doping could be used to enlarge the band gap of a fixed GNR width, resulting in the enhancement of device performances [102].

6 Conclusion

In summary, the present review reports on the basics of electronic and quantum transport properties in low dimensional carbon-based materials including 2D graphene, graphene nanoribbons and carbon nanotubes. Although CNTs and GNRs share similar electronic confinement properties due to their nanoscale lateral sizes, the effects of boundary conditions in the perpendicular direction with respect to the system axis trigger very different electronic and transport properties. For each nanostructure, a simple tight-binding approach (single-band model) has been proposed to describe their specific electronic behavior, and when necessary, ab initio calculations have been used to accurately complete the picture. Both 1D systems have also been perturbed using topological defects (vacancies, adatoms) or chemical doping to taylor their electronic structure. The effect of these topological or chemical perturbations on the quantum transport of both CNTs and GNRs have been predicted.

To conclude, because of their remarkable electronic properties and structural physical properties, CNTs or GNRs are expected to play an important role in the future of nanoscale electronics. Not only can nanotubes be metallic, but they are mechanically very stable and strong, and their carrier mobility is equivalent to that of good metals, suggesting that they would make ideal interconnects in nanosized devices. Further, the intrinsic semiconducting character of other tubes, as controlled by their topology, allows us to build logic devices at the nanometer scale, as already demonstrated in many laboratories. Similarly the combination of 2D graphene for interconnects together with graphene nanoribbons for active field effect transistor devices could allow completely carbon-made nanoelectronics.

The complete understanding of fundamental electronic and transport concepts in low dimensional carbon-based nanomaterials definitely needs for theoretical modeling and advanced quantum simulation, together with joint studies with experiments. Theory has been very important to initiate, validate and orientate carbon nanotube science, particularly as far as electronic properties are concerned. Yet, in 1992 one year after Nanotube discovery by Iijima, several groups theoretically predict their unique behavior as metals or semiconductors. Similarly the electronic properties of 2D graphene and graphene ribbons were explored decades before the fabrication of those nanostructures. Since carbon-based nanomaterials have still probably not revealed all their secrets, numerical simulations have still good days to come in predicting new interesting atomic topologies and their corresponding structural and electronic properties, thus discussing their potential impact in carbon science.

References

1. K.S. Novoselov, A.K. Geim, S.V. Morozov, D. Jiang, S.V. Dubonos, I.V. Girgorieva, A.A. Firsov, Science **306**, 666 (2004)
2. K.S. Novoselov, D. Jiang, F. Schedin, T.J. Booth, V.V. Khotkevich, S.V. Morozov, A.K. Geim, Proc. Nat. Acad. Sci. U.S.A. **102**, 10451 (2005)
3. C. Berger et al., Science **312**, 1191 (2006)
4. P.R. Wallace, Phys. Rev. **71**, 622 (1947)
5. J.-C. Charlier, J.-P. Michenaud, X. Gonze, J.-P. Vigneron, Phys. Rev. B **44**, 13237 (1991)
6. X. Li, X. Wang, L. Zhang, S. Lee, H. Dai, Science **319**, 1229 (2008)
7. X. Du et al., Nature Nanotechnology **3**, 491 (2008)
8. K.S. Novoselov, A.K. Geim, S.V. Morozov, D. Jiang, M.I. Katsnelson, I.V. Girgorieva, S.V. Dubonos, A.A. Firsov, Nature **438**, 197 (2005)
9. Y. Zhang, Y.W. Tan, H.L. Stormer, Ph. Kim, Nature **438**, 201 (2005)
10. M.I. Katsnelson, K.S. Novoselov, A.K. Geim, Nature Physics **2**, 620 (2006)
11. A.K. Geim, K.S. Novoselov, Nature Mater. **6**, 183 (2007)
12. J.-C. Charlier, X. Gonze, J.-P. Michenaud, Europhys. Lett. **28**, 403 (1994)
13. J.-C. Charlier, X. Blase, S. Roche, Rev. Mod. Phys. **79**, 677 (2007)

14. G. Dresselhaus, M.A. Pimenta, R. Saito, J.-C. Charlier, S.D.M. Brown, P. Corio, A. Marucci, M.S. Dresselhaus, in *Science and Application of Nanotubes*, Fundamental Materials Research Series, edited by Tomanek, Enbody (Kluwer Academic, Plenum Publishers, NY, 2000), pp. 275–295

15. S. Reich, J. Maultzsch, C. Thomsen, P. Ordejón, Phys. Rev. B **66**, 035412 (2002)

16. P. Hohenberg, W. Kohn, Phys. Rev. **136**, B864 (1964)

17. W. Kohn, L.J. Sham, Phys. Rev. **140**, A1133 (1965)

18. X. Gonze, J.-M. Beuken, R. Caracas, F. Detraux, M. Fuchs, G.-M. Rignanese, L. Sindic, M. Verstraete, G. Zerah, F. Jollet, M. Torrent, A. Roy, M. Mikami, Ph. Ghosez, J.-Y. Raty, D.C. Allan, Computational Materials Science **25**, 478 (2002)

19. J.M. Soler, E. Artacho, J. Gale, D.A. Garcia, J. Junquera, P. Ordejón, D. Sánchez-Portal, J. Phys.: Condens. Matter **14**, 2745 (2002)

20. N. Troullier, J.L. Martins, Phys. Rev. B **43**, 1993 (1991)

21. J.-C. Charlier, P.C. Eklund, J. Zhu, A.C. Ferrari, Electron and Phonon Properties of Graphene: their Relationship with Carbon Nanotubes, in *Carbon Nanotubes*, edited by A. Jorio, G. Dresselhaus, M.S. Dresselhaus (Springer-Verlag, Berlin, Heidelberg, 2008), Topics Appl. Physics **111**, 673 (2008)

22. K.S. Novoselov, E. McCann, S.V. Morozov, V.I. Fal'ko M.I. Katsnelson, U. Zeitler, D. Jiang, F. Schedin, A.K. Geim, Nature Physics **2**, 177 (2006)

23. S.V. Morozov, K.S. Novoselov, M.I. Katsnelson, F. Schedin, L.A. Ponomarenko, D. Jiang, A.K. Geim, Phys. Rev. Lett. **97**, 016801 (2006)

24. V.M. Galitski, S. Adam, S. Das Sarma, Phys. Rev. Lett. **76**, 245405 (2007)

25. A.H. Castro Neto, F. Guinea, N.M.R. Peres, K.S. Novoselov, A.K. Geim, Rev. Mod. Phys. **81**, 109 (2009)

26. M.Y. Han, B. Ozylmaz, Y. Zhang, P. Kim, Phys. Rev. Lett. **98**, 206805 (2007)

27. L. Tapaszto, G. Dobrik, Ph. Lambin, L. Biro, Nat. Nano. **3**, 397 (2008)

28. K. Nakada, M. Fujita, G. Dresselhaus, M.S. Dresselhaus, Phys. Rev. B **54**, 17 954 (1996)

29. K. Wakabayashi, M. Fujita, H. Ajiki, M. Sigrist, Phys. Rev. B **59**, 8271 (1999)

30. Y. Miyamoto, K. Nakada, M. Fujita, Phys. Rev. B **59**, 9858 (1999)

31. T. Kawai, Y. Miyamoto, O. Sugino, Y. Koga, Phys. Rev. B **62**, R16349 (2000)

32. S. Okada, A. Oshiyama, Phys. Rev. Lett. **87**, 146803 (2001)

33. H. Lee, Y.-W. Sun, N. Park, S. Han, J. Yu, Phys. Rev. B **72**, 174431 (2005)

34. M. Ezawa, Phys. Rev. B **73**, 045432 (2006)

35. L. Brey, H.A. Fertig, Phys. Rev. B **73**, 235411 (2006)

36. K.-I. Sasaki, S. Murakami, R. Saito, J. Phys. Soc. Jpn **75**, 074713 (2006)

37. D.A. Abanin, P.A. Lee, L.S. Levitov, Phys. Rev. Lett. **96**, 176803 (2006)

38. Y.-W. Son, M.L. Cohen, S.G. Louie, Phys. Rev. Lett. **97**, 216803 (2006)

39. Y.-W. Son, M.L. Cohen, S.G. Louie, Nature **444**, 347 (2006)

40. K.A. Ritter, J.W. Lyding, Nat. Mater. **8**, 235 (2009)

41. Z. Liu, K. Suenaga, P.J.F. Harris, S. Iijima, Phys. Rev. Lett. **102**, 015501 (2009)

42. C.O. Girit, J.C. Meyer, R. Erni, M.D. Rossell, C. Kisielowski, L. Yang, C.H. Park, M.F. Crommie, M.L. Cohen, S.G. Louie, A. Zettl, Science **323**, 1705 (2009)

43. P. Koskinen, S. Malola, H. Hakkinen, Phys. Rev. Lett. **101**, 115502 (2008)

44. T. Wassmann, A.P. Seitsonen, A. Marco Saitta, M. Lazzeri, F. Mauri, Phys. Rev. Lett. **101**, 096402 (2008)

45. K. Wakabayashi, Phys. Rev. B **64**, 125408 (2001)

46. N.M.R. Peres, A.H. Castro Neto, F. Guinea, Phys. Rev. B **73**, 195411 (2006)

47. F. Munoz-Rojas, D. Jacob, J. Fernadez-Rossier, J.J. Palacios, Phys. Rev. B **74**, 195417 (2006)

48. H. Zheng, Z.F. Wang, T. Luo, Q.W. Shi, J. Chen, Phys. Rev. B **75**, 165414 (2007)

49. D. Gunlycke, D.A. Areshkin, C.T. White, Phys. Rev. Lett. **90**, 142104 (2007)

50. A. Cresti, N. Nemec, B. Biel, G. Niebler, F. Triozon, G. Cuniberti, S. Roche, Nano Res. **1**, 361 (2008)

51. Y. Kobayashi, K. Fukui, T. Enoki, K. Kusakabe, Y. Kaburagi Phys. Rev. B **71**, 103406 (2005)

52. C.L. Kane, E.J. Mele, Phys. Rev. Lett. **95**, 146802 (2005)

53. G. Dresselhaus, M.S. Dresselhaus Phys. Rev. **140**, 401 (1965)

54. S. Iijima, Nature **354**, 56 (1991)

55. S. Iijima, T. Ichihashi, Nature **363**, 603 (1993)

56. D.S. Bethune, C.H. Kiang, M.S. de Vries, G. Gorman, R. Savoy, J. Vazquez, R. Beyers, Nature **363**, 605 (1993)

57. R. Saito, G. Dresselhaus, M.S. Dresselhaus, *Physical Properties of Carbon Nanotubes* (Imperial College Press, London, 1998)

58. N. Hamada, S. Sawada, A. Oshiyama, Phys. Rev. Lett. **68**, 1579 (1992)

59. R. Saito, M. Fujita, G. Dresselhaus, M.S. Dresselhaus, Appl. Phys. Lett. **60**, 2204 (1992)

60. J.W. Mintmire, B.I. Dunlap, C.T. White, Phys. Rev. Lett. **68**, 631 (1992)

61. C.T. White, J.W. Mintmire, Nature **394**, 29 (1998)

62. R. Saito, G. Dresselhaus, M.S. Dresselhaus, Phys. Rev. B **61**, 2981 (2000)

63. J.W. Mintmire, C.T. White, Phys. Rev. Lett. **81**, 2506 (1998)

64. J.-C. Charlier, Ph. Lambin, Phys. Rev. B **57**, 15037 (1998)

65. J.W.G. Wildöer, L.C. Venema, A.G. Rinzler, R.E. Smalley, C. Dekker, Nature **391**, 59 (1998)

66. T.W. Odom, J.L. Huang, P. Kim, C.M. Lieber, Nature **391**, 62 (1998)

67. L.C. Venema, L.C., J.W.G. Wildöer, J.W. Janssen, S.J. Tans, H.L.J. Temminck, Tuinstra, L.P. Kouwenhoven, C. Dekker, Science **283**, 52 (1999)

68. A. Jorio, A.G.S Filho, G. Dresselhaus, M.S. Dreslhaus, R. Saito, J.H. Hafner, C.M. Lieber, F.M. Matinaga, M.S.S. Dantas, M.A. Pimenta, Phys. Rev. B **63**, 245416 (2001)

69. M.J. O'Connell, S.M. Bachilo, C.B. Huffman, V.C. Moore, M.S. Strano, E.H. Haroz, K.L. Rialon, P.J. Boul, W.H. Noon, C. Kittrell, J. Ma, R.H. Hauge, R.B. Weisman, R.E. Smalley, Science **297**, 593 (2002)

70. S.M. Bachilo, M.S. Strano, C. Kittrell, R.H. Hauge, R.E. Smalley, R.B. Weisman, Science **298**, 2361 (2002)

71. J. Lefebvre, Y. Homma, P. Finnie, Phys. Rev. Lett. **90**, 217401 (2003)

72. C.L. Kane, E.J. Mele, Phys. Rev. Lett. **78**, 1932 (1997)
73. M. Ouyang, J.L. Huang, C.L. Cheung, C.M. Lieber, Science **292**, 702 (2001)
74. G.G. Samsonidze, R. Saito, N. Kobayashi, A. Gruneis, J. Jiang, A. Jorio, S.G. Chou, G. Dresselhaus, M.S. Dresselhaus, Appl. Phys. Lett. **85**, 5703 (2004)
75. V.N. Popov, New J. Phys. **6**, 5 (2004)
76. X. Blase, L.X. Benedict, E.L. Shirley, S.G. Louie, Phys. Rev. Lett. **72**, 1878 (1994)
77. N. Wang, Z.K. Tang, G.D. Li, J.S. Chen, Nature **408**, 50 (2000)
78. Z.K. Tang, L. Zhang, N. Wang, X.X. Zhang, G.H. Wen, G.D. Li, J.N. Wang, C.T. Chan, P. Sheng, Science **292**, 2462 (2001)
79. D. Connétable, G.-M. Rignanese, J.-C. Charlier, X. Blase, Phys. Rev. Lett. **94**, 015503 (2005)
80. R. Kubo, Rep. Prog. Phys. **29**, 255 (1966)
81. M. Büttiker, Y. Imry, R. Landauer, S. Pinhas, Phys. Rev. **31**, 6207 (1985)
82. S. Datta, *Electronic Transport in Mesoscopic Systems* (Cambridge University Press, 1995)
83. A.R. Rocha, V.M. García-Suárez, S.W. Bailey, C.J. Lambert, J. Ferrer, S. Sanvito, Phys. Rev. B **73**, 085414 (2006)
84. D.S. Fisher, P.A. Lee, Phys. Rev. B **23**, R6851 (1981)
85. H.J. Choi, J. Ihm, S.G. Louie, M.L. Cohen, Phys. Rev. Lett. **84**, 2917 (2000)
86. L. Chico, V.H. Crespi, L.X. Benedict, S.G. Louie, M.L. Cohen, Phys. Rev. Lett. **76**, 971 (1996)
87. H. Amara, S. Latil, V. Meunier, Ph. Lambin, J.-C. Charlier, Phys. Rev. B **76**, 115423 (2007)
88. Z. Zanolli, J.-C. Charlier, submitted for publication (2009)
89. S. Latil, S. Roche, D. Mayou, J.-C. Charlier, Phys. Rev. Lett. **92**, 256805 (2004)
90. M. Wimmer, I. Adagideli, S. Berber, D. Tománek, K. Richter Phys. Rev. Lett. **100**, 177207 (2008)
91. S.M.-M. Dubois, G.-M. Rignanese, J.-C. Charlier, submitted for publication (2009)
92. V. Barone, O. Hod, G.E. Scuseria, Nano Lett. **6**, 2748 (2006)
93. C.T. White, J. Li, D. Gunlycke, J.W. Mintmire, J.W. Nano Lett. **7**, 825 (2007)
94. M. Evaldsson, I.V. Zozoulenko, H. Xu, T. Heinzel, Phys. Rev. B **78**, R161407 (2008)
95. E.R. Mucciolo, A.H. Castro Neto, C.H. Lewenkopf, Phys. Rev. B **79**, 075407 (2009)
96. L.G. Cancado, M.A. Pimenta, B.R.A. Neves, M.S.S. Dantas, A. Jorio, Phys. Rev. Lett. **93**, 247401 (2004)
97. Y. Kobayashi, K. Fukui, T. Enoki, K. Kusakabe, Phys. Rev. B **73**, 125415 (2006)
98. Z. Liu, K. Suenaga, P.J.F. Harris, S. Iijima, Phys. Rev. Lett. **102**, 015501 (2009)
99. P. Koskinen, S. Malola, H. Häkkinen, Phys. Rev. Lett. **101**, 115502 (2008)
100. B. Huang, M. Liu, N. Su, J. Wu, W. Duan, B.-L. Gu, F. Liu, Phys. Rev. Lett. **102**, 166404 (2009)
101. V. Derycke, R. Martel, J. Appenzeller, Ph. Avouris, Nano Lett. **1**, 453 (2001)
102. B. Biel, X. Blase, F. Triozon, S. Roche, Phys. Rev. Lett. **102**, 096803 (2009)